Observations during static and cyclic undrained loading of dense Aalborg University sand no. 1

Sabaliauskas, Tomas; Diaz, Alberto Troya; Ibsen, Lars Bo; Nielsen, Søren Dam

Publication date:
2014

Document Version
Publisher's PDF, also known as Version of record

Observations during static and cyclic undrained loading of dense Aalborg University sand no. 1

Tomas Sabaliauskas
Alberto Troya Diaz
Lars Bo Ibsen
Søren Dam Nielsen

ISSN 1901-7278
DCE Technical Memorandum No. 43

DEPARTMENT OF CIVIL ENGINEERING
AALBORG UNIVERSITY

Aalborg University
Department of Civil Engineering
Geotechnical Engineering

DCE Technical Memorandum No. 43

Observations during static and cyclic undrained loading of dense Aalborg University sand no. 1

by

Tomas Sabaliauskas
Alberto Troya Diaz
Lars Bo Ibsen
Søren Dam Nielsen

June 2014

Scientific Publications at the Department of Civil Engineering

Technical Reports are published for timely dissemination of research results and scientific work carried out at the Department of Civil Engineering (DCE) at Aalborg University. This medium allows publication of more detailed explanations and results than typically allowed in scientific journals.

Technical Memoranda are produced to enable the preliminary dissemination of scientific work by the personnel of the DCE where such release is deemed to be appropriate. Documents of this kind may be incomplete or temporary versions of papers—or part of continuing work. This should be kept in mind when references are given to publications of this kind.

Contract Reports are produced to report scientific work carried out under contract. Publications of this kind contain confidential matter and are reserved for the sponsors and the DCE. Therefore, Contract Reports are generally not available for public circulation.

Lecture Notes contain material produced by the lecturers at the DCE for educational purposes. This may be scientific notes, lecture books, example problems or manuals for laboratory work, or computer programs developed at the DCE.

Theses are monograms or collections of papers published to report the scientific work carried out at the DCE to obtain a degree as either PhD or Doctor of Technology. The thesis is publicly available after the defence of the degree.

Latest News is published to enable rapid communication of information about scientific work carried out at the DCE. This includes the status of research projects, developments in the laboratories, information about collaborative work and recent research results.

Published 2014 by
Aalborg University
Department of Civil Engineering
Sohngaardsholmsvej 57,
DK-9000 Aalborg, Denmark

Printed in Aalborg at Aalborg University

ISSN 1901-7278
DCE Technical Memorandum No. 43

Observations during static and cyclic undrained loading of dense Aalborg University sand no. 1

Tomas Sabaliauskas, Alberto Troya Diaz, Lars Bo Ibsen, Søren Dam Nielsen

Abstract
Offshore structures are subjected to cyclic loading, which is one of the most important factors in the foundation design. Cyclic loading lead to complex soil response in undrained conditions. In this paper dense Aalborg University sand no. 1, $I_D = 90$ %, is investigated performing a series of monotonic and cyclic triaxial tests. The post-cyclic strength is tested in the specimens that did not fail during the cyclic test.

Dense sand under undrained conditions is found to have more strength than in drained. An increase of 29 % in the shear strength of the soil due to cyclic loading is observed. Soil strength and stiffness are found to change depending on the type of loading applied.

Effective friction angle is found to be changing during various phases of loading. Linear Mohr Coulomb model could potentially be sufficient for modeling the full spectrum of dense sand behavior if extended with a changing friction angle following the examined patterns of response.

A total stress path based material model is presented in this paper.

Keywords
undrained; dense sand; strengthening; cyclic; after load; monotonic; dynamic; friction angle; Mohr Coulomb

Department of Civil engineering, Aalborg University, Denmark

Introduction

Offshore structures often undergo rapid, cyclic loading such as the storms induced wave loads. The seabed is tipically composed of dense sand. Under rapid loading the soil sourrounding the foundation could experience an undrained reaction. In this conditions dense sand shows a very complex behaviour where strengthning, weakening and changes in the stiffness of the soil are present. Nowadays there are no robust and fully reliable methods to model the soil response for dense undrained sand.

A new fatigue theory for sand has been developed in the last 25 years, in which the setup used in static and cyclic triaxial tests has been modified in order to get homogeneous stress and strain conditions which allows to observe more correct soil responses, [Ibsen, 1993]. In the following years the Characteristic Line (CL) and the Cyclic Stable Line (CSL) were described in [Ibsen, 1994]. Previous work in dense sand was done in [Andersen and Berre, 1999] and [Andersen, 2009], in which a design diagram for cyclic loading is presented. Furthermore in undrained conditions previous work is presented in [Nielsen et al., 2013], in which the undrained shear strength is found to be dependent on the initial pore pressure and the initial mean effective stresses.

This paper is dedicated to get insight into undrained response of dense sand. The dynamics of the stress paths observed are described, specially attention is given to one-way compression loading, two-way loading and one-way extension loading. Linear Mohr Coulomb soil model will be used in the description of the observed phenomena and to deal with the position relative to the drained failure envelope.

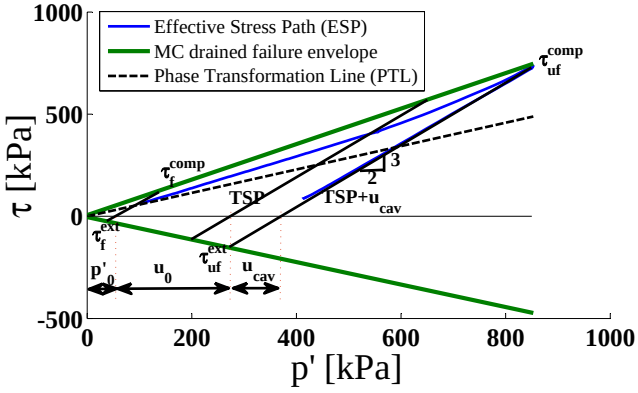

Figure 1. Illustration of the effect of initial pore pressure, initial mean effective stress and pore pressure at cavitation to the drained failure criterion in undrained conditions.

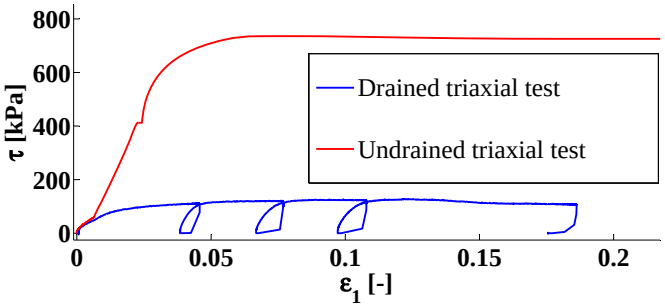

Figure 2. Comparison of the drained and the undrained shear strength of a soil element of dense Aalborg university sand no. 1 from triaxial tests performed at the Geotechnical Laboratory, [Troya et al., 2014].

1. Undrained shear strength of dense sand

For dilative soils undrained shear strength is known to be larger than the drained shear strength due to an increase of the mean effective stresses. The undrained shear strength (τ_{uf}) is dominated by the initial conditions of the soil such as initial mean effective stresses (p_0') and intial pore pressure (u_0), and by the cavitation limit (u_{cav}), as illustrated in Figure 1. In both cases the same drained failure envelope limits the sample strength, but is reached in a different stress state. Hence the difference in the strength comes from the way the stress path develops during loading.

In the drained case the drained failure envelope is reached by a line with a slope of $\frac{3}{2}$ from initial stress point $p_0\prime$. In the undrained case the failure envelope is reached by a line with a slope of $\frac{3}{2}$ in the from the point $p_0\prime + u_0 + u_{cav}$, where $p_0\prime$ is the initial confining pressure, u_0 means the initial pore pressure which simulates the water depth and u_{cav} is the water cavitation pressure ($\approx |-95|$ kPa). In Figure 2 it is illustrated the shear strength in drained and undrained conditions from two triaxial compression tests.

The shear strength has been shown to increase if the initial pore pressure is increased. Thus a sample that initially is under 100 m of water pressure will have a longer stress path along the hydrostatic line than a sample with a 1 m initial state water column, as explained in [Ibsen, 1995] and[Nielsen et al., 2013].

The drained failure envelope in compression and extension can be described by Equations 1 and 2 respectively.

$$\tau_f^{comp}(p') = \frac{3\sin(\phi')}{3-\sin(\phi')}\left(p' + c\cdot\cot(\phi')\right) \tag{1}$$

$$\tau_f^{ext}(p') = \frac{-3\sin(\phi')}{3+\sin(\phi')}\left(p' + c\cdot\cot(\phi')\right) \tag{2}$$

In undrained case τ_f^{max} and τ_f^{min}, instead of a linear envelope are a constant maximum and minimum level, which can also be called a point, as it results from two lines (drained failure envelope and $TSP + u_{cav}$ line) coinciding.

$$\tau_f^{max} = -\frac{(c\cdot\cos(\phi') + p_0^{tot}\cdot\sin(\phi'))}{\sin(\phi')-1} \tag{3}$$

$$\tau_f^{min} = -\frac{(c\cdot\cos(\phi') + p_0^{tot}\cdot\sin(\phi'))}{\sin(\phi')+1} \tag{4}$$

$$p_0^{tot} = p_0' + u_0 + u_{cav} \tag{5}$$

1.1 Mobilization index

Various models try to approximate properties in proportion of how close to failure the loading gets. Just like the failure surface can be described by angle ϕ, so can a second surface indicating a phase transformation line, (PTL). Further detailing can show angles of parameters like stable state line (SSL), or cyclic stable line (CSL). Many surfaces can be used to partition the stress space into different reaction inducing zones.

Currently the state of the art multiple yield surface models are Prevost and similar, which are based on interpolating the volumetric increment with a continuous distribution function in principal stress space, see [Yang et al., 2003] and [Cerfontaine et al., 2013].

In [Ibsen, 1991] an approach to describe the position of a point in the stress space with a mobilization index M is introduced, see Equation 6. There are two ways of evaluating mobilization, M and Mob.

$$M = \frac{q}{|q_f(p')|} = \frac{\tau}{|\tau_f(p')|} \tag{6}$$

(7)

M is equal to 1 when the soil effective stress state at the compressive failure envelope (anywhere on the failure envelope), 0 when shear stress is 0, -1 when touching the extension failure envelope. A modified version of the mobilization index, Mob, is introduced in this paper and represents the amount of total strength being mobilized. In undrained case a value of $M \approx 0.95$ is kept through most of the dilation happening along the common stress path (CSP). Mob increases linearly independent of the angle and is connected only to the final maximum and minimum resistance.

$$\text{If } \tau(t) > 0 \,;\, Mob = \frac{\tau(t)}{\tau_{uf}^{comp}} \tag{8}$$

$$\text{If } \tau(t) < 0 \,;\, Mob = \frac{-\tau(t)}{\tau_{uf}^{ext}} \tag{9}$$

The difference is illustrated in Figure 3 in which it can be seen that the modified mobilization index, Mob (Figure 3b), has a vertical gradient while M (Figure 3a) is distributed along the angle.

Using mobilization allows to compensate for the asymmetric MC failure envelope, i.e., the maximum shear stress is

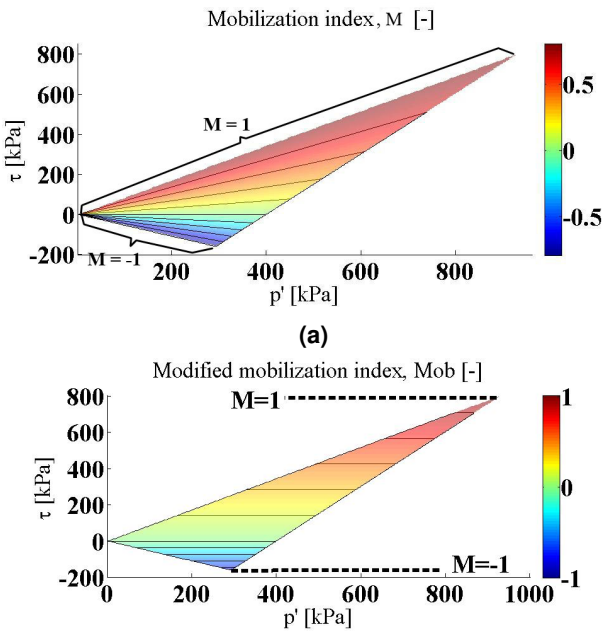

Figure 3. Mobilization index M and modified mobilization index Mob.

larger in compression than in extension, see [Praastrup et al., 1999] and [Ibsen and Praastrup, 2002]. The distribution of some properties along the modified mobilization index, Mob, will be used in the total stress based material model presented in this paper.

1.2 Stress angle

A coefficient called stress ratio is used to describe the behaviour of the soil in [Yang et al., 2003]. However an angular expression is easier to interpret in visual 2-dimensional plots. Thus in this paper it is introduced a new variable based in the stress ratio, the stress angle. The stress angle, η, is defined by Equation 10 as the angle between applied shear stress and zero stress axis with respect to the zero shear resistance point in linear Mohr-Coulomb model, see Figure 4.

$$\eta = \arctan\left(\frac{\tau}{p' + \cot(c)}\right) \tag{10}$$

The stress angle is always less than the friction angle. During dilation the position of stress angle is slightly below failure, following the common stress path, (CSP). According to [Ibsen, 1994], the induced level of dilation is on a semi-constant mobilization index position. Thus following the stress path along during dilation can provide insight into failure envelope movement with each cycle.

2. Multi-yield surface material models

Multi-yield surface material models try to reproduce the behaviour of a material by distributing the stress space into

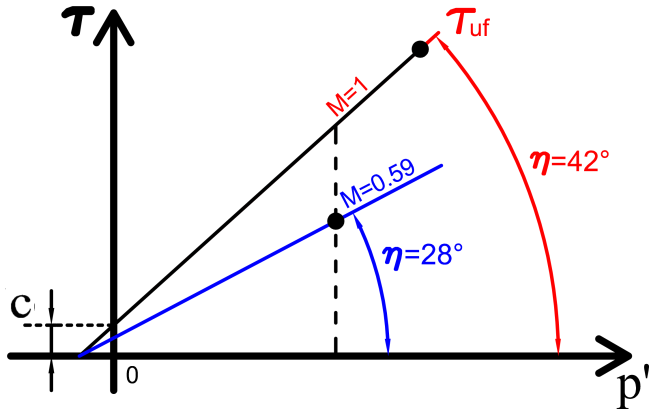

Figure 4. Definition of stress angle, η.

multiple sections with different parameters. Indeed it is often the case that soil material models are described by a variety of lines that either follow a line or are parallel to a line such as phase transformation line (PTL), common stress path (CSP), failure envelope, stable state line (SSL)... and each surface has isotropic or kinematic hardening, see Figure 5. Some forms of this type of partitioning are found to be unavoidable when modeling cyclic loading, see [Ishihara, 1996] and [Yang et al.,

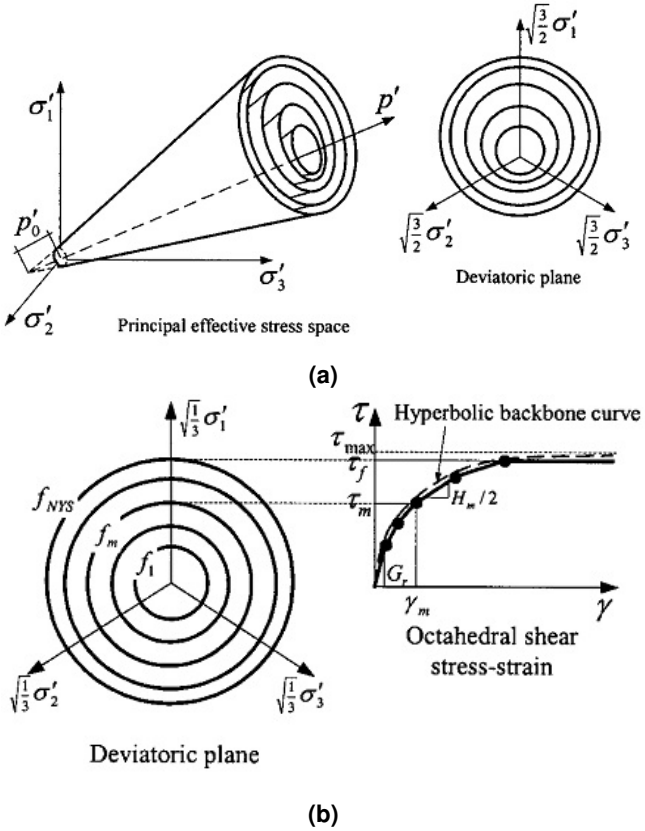

Figure 5. Multi-surface model a) in 3-D and b) deviatoric plane view, [Yang et al., 2003].

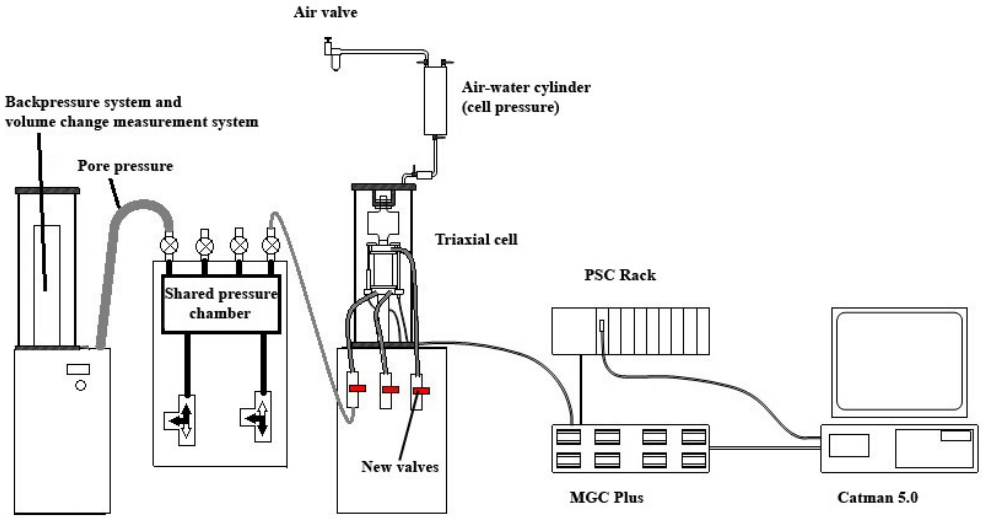

Figure 6. Sketch of the triaxial setup at Geotechnichal Laboratory at Aalborg University.

2003].

It is of importance for modeling cyclic behaviour to find a distribution of values along the deviatoric stress space. This allows to reach a smoother curve along the angle, with less variables to keep track of. An illustration of shear stiffness being distributed along the deviatoric plane is given in Figure 5b.

Equation 11 shows an approximated distribution of contractile behaviour. P'' represents a volumetric strain. In this paper only pore pressure is measured, but pore pressure is nearly linearly proportional to volume change. Thus fitting a curve on pre-cavitation pore pressure distribution can be done, and if the exact volume change is of interest - a coefficient of bulk stiffness can be used to convert the pore pressure change into volume strain. The same goes for Equation 12, where dilation is approximated. This two equations are presented in [Yang et al., 2003].

$$P'' = [1 - sign(\dot{\eta})\eta/\eta_{PT}](c_1 + c_2\varepsilon_c) \quad (11)$$

$$P'' = [1 - \eta/\eta_{PT}](d_1(\gamma_d)^{d_2}) \quad (12)$$

where:

c_1,c_2,d_1,d_2	-fitted constants.
γ_d	-accumulated strain.
ε_c	-scalar function that describes volume strain.

Plots that involves stiffness and pore pressure distributed along the stress angle allows to see the evolution of the shapes and the changes as functions of these parameters. This is a key point when fitting data on a stress angle dependent material model.

This set of rules can capture some of the cyclic behavior, but measurements found during testing indicate that it is incomplete. Using accumulated strain as the key parameter does not allow to model load-induced hardening. A concept of using efficiency of a soil skeleton instead of accumulated strain is suggested later in this paper. Efficiency is dependent on stress history and can be used for scaling both the dilation and contraction response.

3. Test setup

The modern dynamic triaxial setup at Aalborg University allows to perform highly accurate dynamic triaxial tests on sand. The tests are prepared according to the procedure described in [Shajarati et al., 2012]. In Figure 6, a sketch of the setup is illustrated in which three valves that separate the shared pressure chamber from the specimen are highlighted in red. These are added with the purpose of reducing the volume of water that remains in the cables and also accounts for a more comfortable use of the setup. Furthermore it allows to mount a second latex membrane and hence increasing the efficiency in the testing procedure, see [Troya and Sabaliauskas, 2014].

According to [Ibsen, 1993], the tests are run on specimens of height equal to the diameter - of 70×70 mm - and with smooth plates to ensure homogeneous stress and strain conditions. The displacements in the specimen are measured with two displacement transducers attached directly to the top and bottom plates of the specimen which allows to measure the real strain of the sample without pollution of the whole system deformation. In this article the displacements of the specimen are converted to engineering strain, as relatively small strains are of interest.

The soil used for the tests is Aalborg University sand no. 1 with a $I_D = 90$ % obtained applying dry tamping technique, see details in [Troya and Sabaliauskas, 2014]. The specimens are anisotropically consolidated to a vertical effective stress of $\sigma_v\prime = 171.5$ kPa, meaning that for a coefficient of lateral

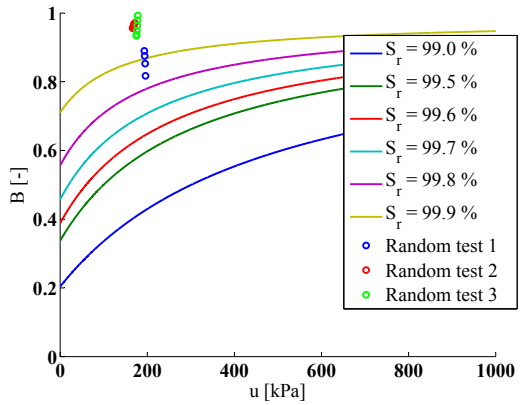

Figure 7. Skempton's B values of 3 random tests of the series.

earth pressure at rest of $K_0 = 0.35$, the horizontal effective stress during consolidation should be $\sigma_h\prime = 60$ kPa. It was mentioned before that the amount of water in the system is reduced by reducing the cable length, which has an influence in the saturation of the sample: values of Skempton's B test above 99.9 % of saturation level are obtained. This is illustrated in Figure 7 with 3 random tests of the series. The initial pore pressure is set up to $u_0 = 200$ kPa by using the backpressure system. In this way an element placed 20 m below the mean water level is to be reproduced.

Loading starts from a K_0 loading being applied in drained conditions over a period of 1 hour and kept in drained conditions until no strain creep is identifiable. Then the valves are closed and data recording is initiated for undrained response. The average cyclic load is applied in undrained conditions in approximately 11 seconds. After few seconds in this state the cyclic load is initiated. Each test consisted of up to 1000 cycles of sinusoidal loading of chosen amplitude and mean value. If the specimen did not develop a failure surface and shear strain γ never reached 15% - the sample was further tested for the resulting strength by ramp loading to failure.

3.1 Loading control

The loading system used in the tests, MOOG Plus, offers two different options for control the loading applied: displacement and force.

Position control uses the displacement transducer data to push or pull on the piston. It is very robust and can catch the goal position in time with extreme precision.

Force control is more complicated as the system has to apply a displacement that will provide the necessary force, controlled by a force transducer that provides a feedback to the loading system.

Unfortunately sand specimens have very unstable stiffness at specific times. This is mostly limited to instances where the loading goes through the 0 shear stress line where the sample tends to liquefy but the fine tuned state of the art MOOG control system handles this quite well.

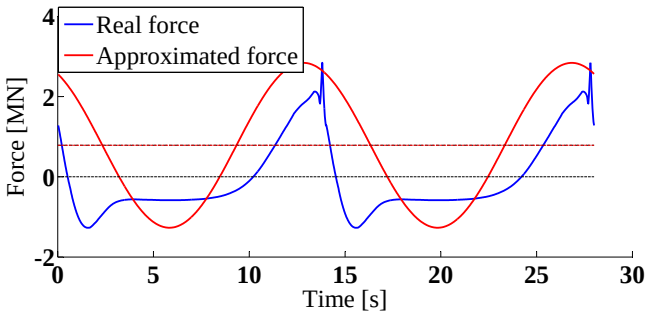

Figure 8. Approximation of the force on a wind turbine during the 50-year event of an offshore storm in the North Sea, [Troya et al., 2014].

Cyclic loading is parameterized by the shear stress amplitude τ_{cy} and the average value τ_a which simulate the loading shape in an offshore structure as illustrated in Figure 8, giving a response of a permanent value of the shear strain γ_p and a cyclic shear strain γ_{cy} as illustrated in Figure 9.

4. Triaxial tests

In this paper 2 monotonic tests and 7 cyclic triaxial tests of the series are described in detail and are highlighted in grey in Table 1, in which the loading parameters of the tests, the initial pore pressure as well as the number of cycles to failure and the post-cyclic strength when applicable are presented.

4.1 Loading-up and loading-down

In this paper it is of importance to differ in the illustrations between loading-up and loading-down. Loading-up is when the value of applied load is increasing. In the colored plots this part of loading phase is always plotted in blue. The sign of the derivative of the force, $\dot{F}$, is used to differentiate between loading-up and loading-down. It corresponds to cases

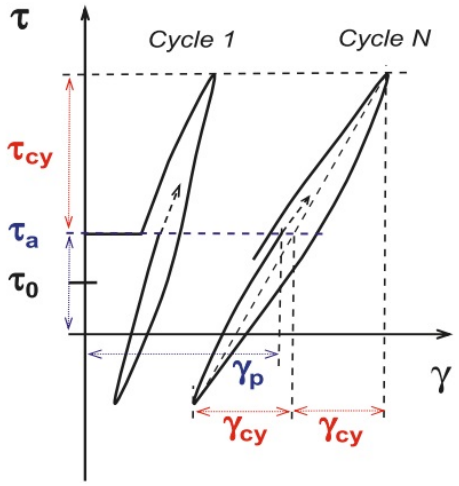

Figure 9. Stress-strain behaviour under cyclic loading, [Andersen and Berre, 1999]

Test No.	τ_a [kPa]	τ_{cy} [kPa]	u_0 [kPa]	N_f [−]	τ_{uf}^{post} [kPa]
1	56	59.7	200	1000	643.2
2	55.5	123.3	200	106	-
3	−134.3	-	200	-	-
4	56.5	183.8	200	10	-
5	186.2	316.3	200	2	-
6	252.3	383.4	200	4	-
7	46.2	133.3	200	81	-
8	0.9	4.8	200	1000	-
9	288.3	388.7	200	59	-
10	52	185	200	6	-
11	53.4	150	200	81	-
12	−0.4	136.2	200	4	-
13	418.7	123.4	200	1000	796.9
14	325.3	315.4	200	1000	-
15	361.8	351.4	200	1000	933.3
16	735.8	-	200	-	-
17	377.3	366.2	200	1000	949.5
18	516	217.6	200	1000	836.6
19	−63.4	50.4	200	1000	786
20	−63.5	50.4	200	1000	−130.6
21	305.5	425.5	200	15	-
22	0	61.3	200	225	-

Table 1. List of triaxial tests run at the Geotechnichal Laboratory at Aalborg University.

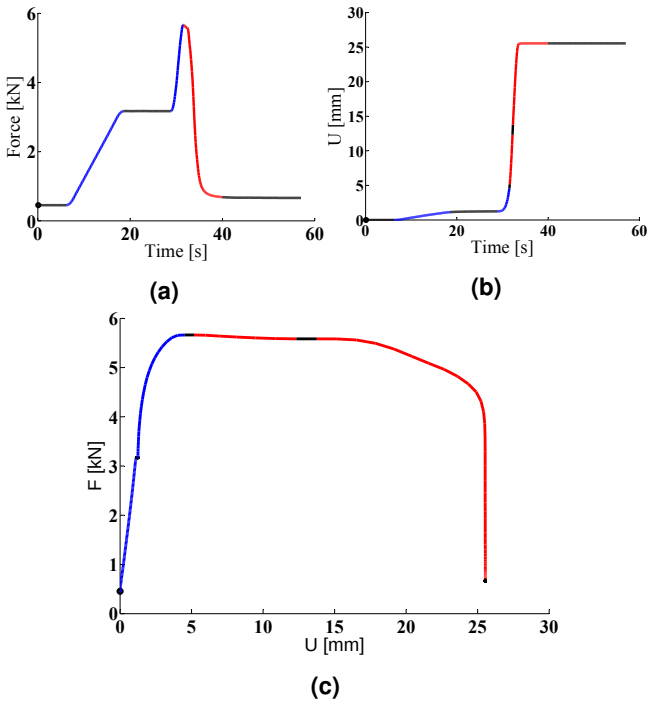

Figure 10. Loading and displacement curves of test no. 16. a) Force timeseries, b) displacement timeseries c)force-displacement curve.

where $\dot{F} > 0$. Loading-down is when the applied load is being decreased and in this paper it will be plotted in red. Opposed to loading-up, loading-down corresponds to $\dot{F} < 0$. The cases when the load is constant and therefore $\dot{F} = 0$ will be plotted in black. The beggining of the loading is marked by a black circle in all the plots.

5. Monotonic loading

Monotonic loading serves as a good example to get comfortable around the color coding, which simplifies further descriptions of observed reactions and to familiarize with the plots selected in this paper that help to describe dense sand behaviour.

5.1 Monotonic compression

Loading - Force control

This test corresponds to the test no. 16 in Table 1. In this case force control loading is used. It is represented in Fig.10a. In this specific example the tested sample failed during the first quarter of the first cycle. The maximum loading force reached can be seen in Figure 10a and is close to 6 kN. Excessive displacements can be seen in Figure 10b which were developing during the peak load. Plasticity is easily identified from the curve in Figure 10c. From this very first graph it can be seen that shear strength of soil is decreasing as failure progresses. Later it is shown how the friction angle of sand is dropping with a weakening sample during cyclic loading.

Stress and strain

Shear and confining stresses are used in linear Mohr-Coulomb models. The thickest black line on the left in Figure 11a is the envelope given by Equation 1 and the one on the right in the same figure represents the total stress path plus cavitation pressure, $TSP + u_{cav}$. The red loading-down path coincides with it, covering it almost completely. It can be observed how the loading-up path in blue rises close to the failure envelope, following a constant angle path. That angle is close to 0.94 in mobilization index. At some point it starts deviating towards the failure envelope. This happens as cavitation starts to take place when the pore pressure gets close to −100 kPa.

In Figure 11b plasticity can be clearly noticed. The coordinates of deviatoric stress q=$\sigma_1 - \sigma_3$ and $\varepsilon_{vert} = \Delta U / H_{sample}$ are chosen because of lack in precision of measuring Poisson's ratio. It is well known that in undrained loading case Poisson's ratio $\nu \approx 0.5$. However during cavitation soil takes up a hugely non linear shift in Poisson's ratio which it is often approximated rather than measured, see [Ishihara, 1996]. It was chosen to stay away from arbitrary approximations as much as possible in this paper.

In Figure 11c the changes in the pore pressure with respect to the vertical strain are illustrated. The volume change is proportional to the pore pressure change. In undrained conditions the volume change is extremely small and the exact volumetric stress to strain ratio is not known. In this plot it can be

observed in which direction the sample volume is heading and what state the pore pressure is. It is obvious that during the final stages of loading-up (blue line) cavitation is gradually reached and stabilizes close to −100 kPa. It is important to notice that the sample keeps dilating past this point, but the water now became into a gas, thus the volume can expand.

This continued dilation past the cavitation point is responsible for the return path going down with a slope of $\frac{3}{2}$ -red line- as seen in Figure 11a. This path will later on be shown to result in the cyclic soil strengthening. The tests that lie in this path reach higher levels of confining stress at lower levels of shear stress, thus resulting in hardening. Hardening is often modeled by a hardening law that involves various failure criterion that have a hardening 'cap' limit, compared to the stress paths resulting from a non-critical, non-cavitating level, loading response as shown in Figure 1. Dilation is modeled as a function of strain during a specific stress state. It also may be used to set the limits for 'energy capacity' - serving as a limit to how much a sample can dilate, as well as be used directly for parameterizing a cyclic loading response, see [Ishihara, 1996] and [Yang et al., 2003].

Notice how the blue and red color mapping allows to distinguish where the loading-up stops but deformations continue even during loading-down. Peak stress state values are not in the same position as peak deformation. For instance in Figure 11b, red line shows plastic deformation continues even after loading-up is finished and an elastic response during loading-down begins only at around 1100 kPa closer to the middle of loading-down.

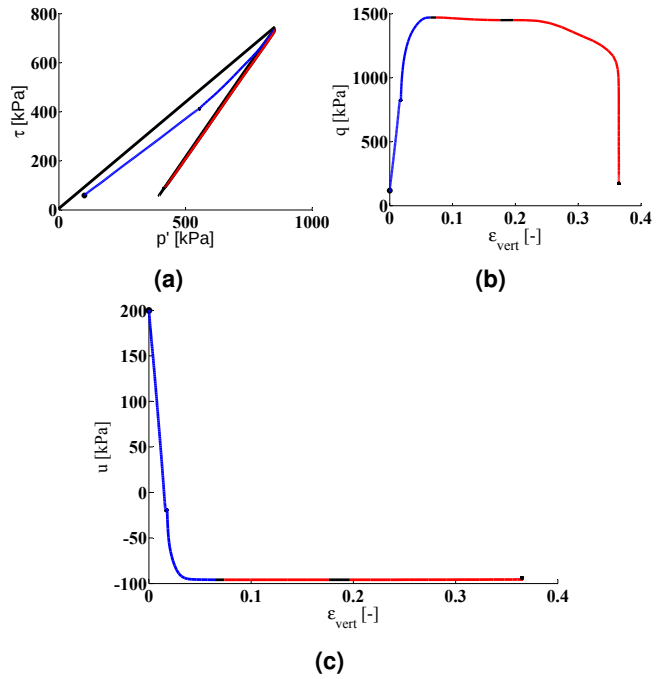

Figure 11. Stress and strain curves of test no. 16. a) Stress path in p'-τ space, b) Stress-strain curve, c) Pore pressure-strain curve.

Volumetric strain in stress space

Volume change can be considered neglegible in undrained tests. However it has a big influence on the pore pressure. It is usually accepted to take a Poisson's ratio of ≈ 0.5 before cavitation takes place due to water being highly incompressible, but since this paper describes the phenomena transitioning between drained and undrained regimes (when water cavitates) Poisson's ratio becomes highly non linear. As it was mentioned before pore pressure gives a proportional measure of volume change inside the specimen.

Volume change in the specimen is important as it represents alterations in the density which is the main factor that parameterizes the soil strength, [Andersen and Berre, 1999]. In modeling practice it is important to find the distribution of dilation and contraction along the stress angle and confining stress as these parameters are most often used to describe dilating and contracting effects during a strain increment, as seen in [Yang et al., 2003], [Ishihara, 1996], [Ibsen, 1991] and [Helwany, 2007].

It was noticed that the notation of using density alone is insufficient to cover the full range of obervations. In undrained tests the volume change is minuscule, density can be considered constant and still, there is a wide range of changes in strength, stiffness and volumetric response within the sample. Adding the notation of soil skeleton "efficiency" which is meant for quantifying sand particle arrangement, allows to approach towards a closed-form solution of observed soil behaviour.

In Figure 12a pore pressure related to the stress angle is shown. Pore pressure is initiated at 200 kPa and further develops due to volumetric changes in the sample. The initial stress state is already above the phase transformation line (PTL) and dilation induced drop in pore pressure is visible. Tangent of the curve becomes horizontal at some point, indicating that a near constant angle in the principal stress space is maintained. As dilation kicks in the stress angle closes in towards the effective friction angle. After the load is removed pore pressure does not drop as soil skeleton voids do not contract enough to compensate for water vaporizing into a gas.

In Fig.12b it is seen that the soil skeleton is subjected to a great confining stress. During loading-up the stress state is highly dominated by shear dilation. During loading-down the stress state shifts towards a more isotropic confining state and a slight tendency towards increasing in pore pressure is present which indicates that the volume is decreasing and sample density is increasing. During cyclic loading it will become obvious that going past the zero deviatoric stress results in increasing level of compression in the voids. Measurements show that while one-way loading result in some form of a grain distribution, that becomes more efficient in carrying the load applied, two-way loading seems to prevent formation of any sort of load bearing particle structure.

The last plot in this figure, see Figure 12c, is meant to show how the stress angle is changing during the loading

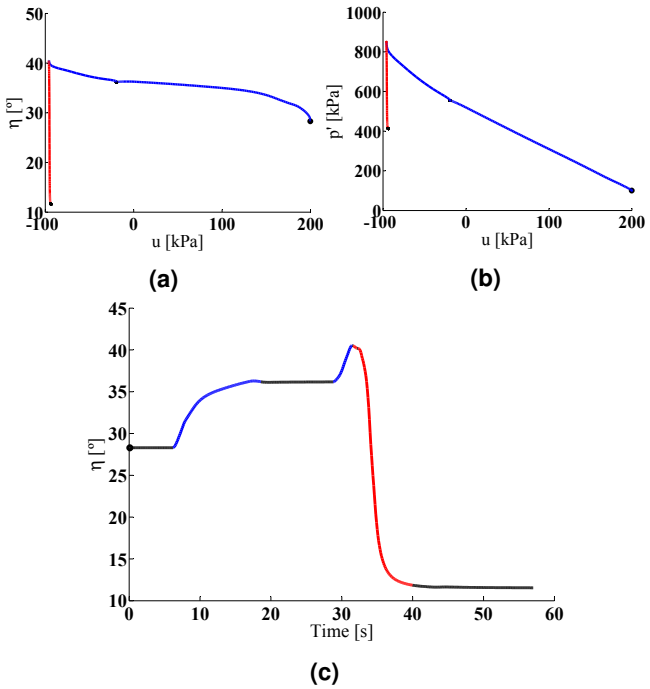

Figure 12. Pore pressure curves of test no. 16. a) Pore pressure distribution along stress angle, b) pore pressure distribution along mean effective stress, c) stress angle timeseries.

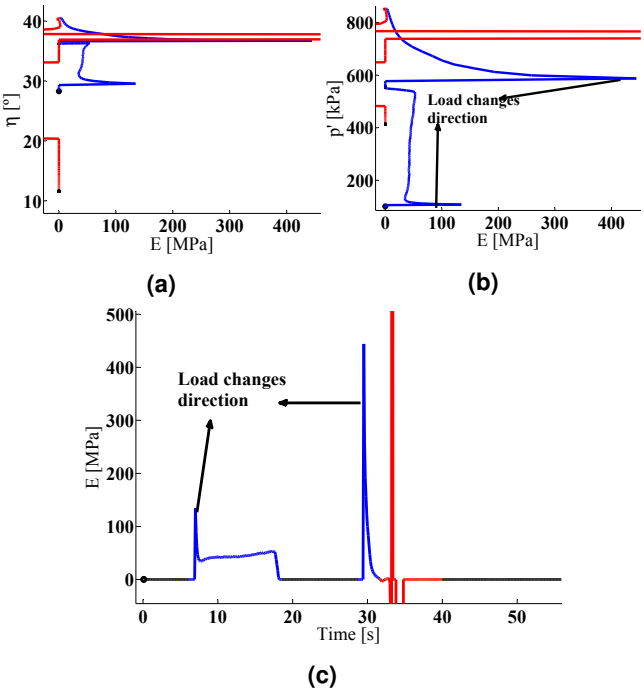

Figure 13. Stiffness curves of test no. 16. a) Stiffness distribution along the stress angle, b) Stiffness distribution along the mean stress, c) Stiffness timeseries.

in time. In cyclic loading cases an increase or decrease in ultimate friction angle, or rather in the 'common stress path' angle is noticeable. In the monotonic case it is worth noticing that dilation happens following a rather constant angle. This is true before the grain distribution in the skeleton is influenced. Thus a constant ultimate friction angle is valid for a monotonic load.

Stiffness

Stiffness is a very important parameter of all numerical modeling. Thus it makes sense to look for some common patterns in stiffness distribution along commonly used parameters and get accustomed to how stiffness develops over a loading sequence. A positive stiffness increment indicates elastic component to be present, zero means pure plasticity and negative means relaxation or creep dominant reaction. This can give valuable insight in what is happening along the friction angle, confining stress state or through loading history.

Here the tangent stiffness modulus increment, $E = \frac{\Delta q}{\Delta \varepsilon_{vert}}$, is plotted as a stiffness parameter, as it is the closest plausible measure of instantaneous stiffness.

In Figure 13a the stiffness increments on the horizontal and the stress angle on vertical axis are shown. The stress angle is used to parameterize the failure envelope, and is thus correlated with decreasing stiffness in most modeling situations. This assumption is confirmed in the second half of the loading after the second extreme peak in blue, where angle is rising and increment stiffness is dropping, meaning that plasticity is developing gradually as the failure envelope is approached.

In Figure 13b, stiffness is on the horizontal again and confining stress is on the vertical axis. Confining stress along the hydrostatic axis is the 'strengthening' parameter in the drained case. When it is dominant there is supposed to be an increase in strength. A tendency of increasing stiffness while moving up the hydrostatic axis is noticeable during the first part of the load, where the angle is kept relatively constant, confirming the assumption. This struggle between the two strengthening and weakening factors, dilation and contraction, is the back bone of cyclic soil behavior. In the undrained loading scenario dilation rearranges the grains which can make the spacing either stronger or weaker.

In Figure 13c the timeseries of the stiffness is plotted. It can be noticed that the stiffness increases during the last part of the loading-up. It is noticed in all the plots in Figure 13 that every time the loads change direction a peak in the stiffness is obtained. There is a big influence of creep noticeable.

5.2 Monotonic extension

Extension is limited by the same principle of failure as compression. The line of $TSP + u_{cav}$ is touching the linear envelope in the negative side of shear stress, see Figure 1.

Loading - Displacement control

This test corresponds to the test no. 3 found in Table 1 in which displacement controlled loading was chosen as loading control. This is the only displacement controlled test of

Figure 14. Illustration of failure in extension of test no. 3.

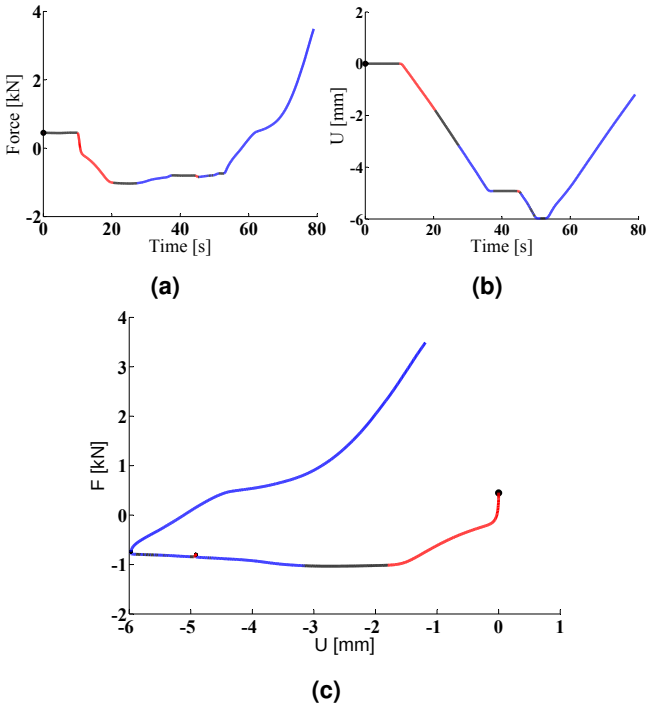

Figure 15. Loading and displacement curves of test no. 3. a) Force timeseries, b) displacement timeseries c)force-displacement curve.

the series. Displacement control allows to observe the relaxation modulus at times of constant strain, instead of creep at constant stress.

Displacement control graph is shown in Figure 15b. The triaxial setup used has the limit capacity to pull on the sample a maximum of 6 mm. Sample in this loading case partially failed in extension by developing a very mild crack indicating a failure mechanism might be developing, see Figure 14. The deformations were not extreme and loading was continued in compression displacement to get some data on reverse loading behavior. Loading-up and loading-down color scheme in the force timeseries in Figure 15a indicate at what points the reaction force changes its direction while the displacement is being applied.

From the plot in Figure 15c it is visible that reaction force gradually drops as induced displacements continue after loading. The increment tangent stiffness indicates to be negative at this point. It is important to distinguish the difference in increment and the model stiffness here. Increment stiffness is due to failure envelope changing. System stiffness is the stiffness that would be there if the whole elastic amplitude was measured.

Red line in extension represents quite clearly distinguishable phases of elasticity, elasto-plasticity and pure plasticity, as the $F-U$ slope changes. The slope changing into a negative stiffness increment after -3 mm here is nothing more than the failure envelope narrowing down. This can be modeled by including a decreasing friction angle as dilation decreases sample density during cavitation. When applied displacement direction changes very brief recovery of elastic stiffness can be observed and an elasto-plastic angle repeats itself after, way up until ≈ -4.5 mm. From there on a pure plastic response is gradually rising in stiffness.

Stress and strain

Mohr-Coulomb stress space in Figure 16a show a very nice case of loading-down stress path starting out in a elastic mode, then dilating along the CSP and stopping at the $TSP+u_{cav}$ line. When uploaded the stress path locks in to the $TSP+u_{cav}$ line due to slight excess dilation. As the stress state approaches hydrostatic axis the resulting confining pressure force the voids to start contracting, and after compression is added, the sample goes through all the stages of contraction, dilation and ultimately failure. Failure occurs at a noticeably decreased friction angle than the sample has in initial conditions.

In Figure 16b it is illustrated the deviatoric stress acting to elongation and the three phases - elastic, elastoplastic and pure plastic - are again clearly defined in extension and compression. The elasto-plastic part can be seen to have stayed close to the same strain. Stiffness tangent can be seen to be increasing rapidly as the stress state climbs up along the hydrostatic axis, with elongation being limited by recovered water stiffness preventing dilation.

The third graph of the series corresponds to Figure 16c which shows how pore pressure changes as elongation progresses. Volumetric strain is a function of strain, activated when stress angle reaches critical values. Pore pressure reacts close to linearly towards dilation up until cavitation takes place. From drained tests it is known that dilation continues

further, after cavitation level is reached together with continuing strain development. When the applied strain direction is reversed the voids start closing and the water condensates back into a fluid state. A new maximum density is reached at approximately $\varepsilon_{vert} = -0.045$, where contraction inducing stress angle is overtaken by dilation effect.

Volumetric strain in stress space

Pore pressure is plotted along the stress angle Figure 17a. It is clearly visible how well dilation is described during extension. It follows an almost constant stress angle up until cavitation. It is generally accepted to describe the position where contracting properties transition into dilation through a phase transformation line positioned in the Mohr-Coulmb space. When comparing the plots of Figure 17a and Figure 17b it can be observed that during the recovery of pore pressure a nearly straight line, with the same slope as during dilation is followed way up until the next dilation dominant path is reached. It is this kind of linear patterns that often reveal convenient relations between values of interest. It serves as good reason to look for correlation between confining stress and pore pressure recovery as this is a very troublesome even in most advanced numerical simulations at the moment.

In the stress angle timeseries shown in Figure 17c it is visible how the friction angle starts dropping after failure in extension is reached.

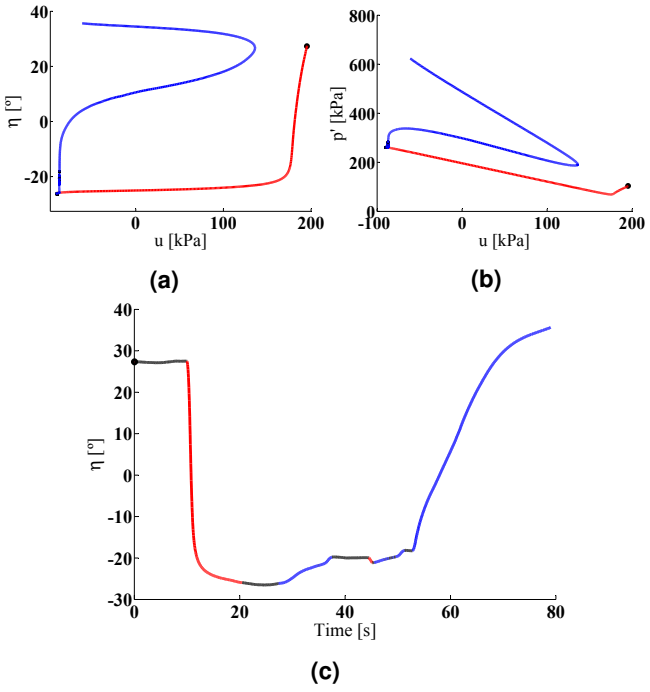

Figure 17. Pore pressure curves of test no. 3. a) Pore pressure distribution along stress angle, b) pore pressure distribution along mean effective stress, c) stress angle timeseries.

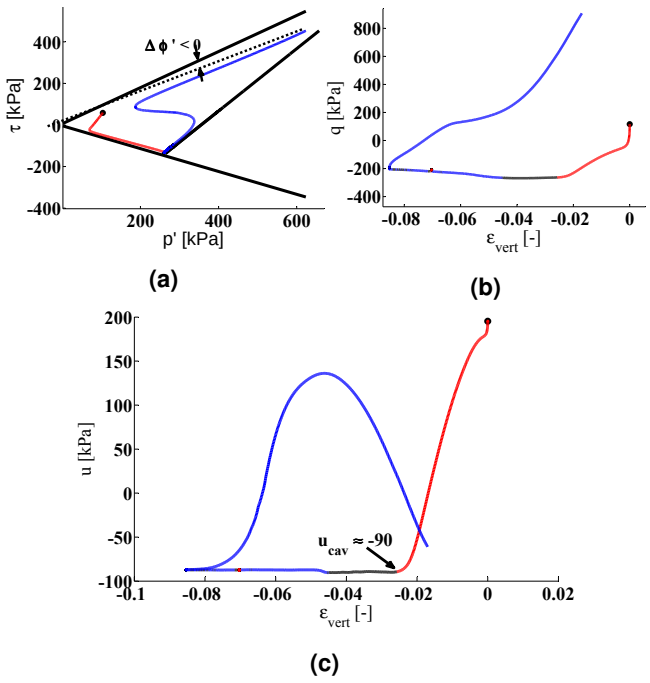

Figure 16. Stress and strain curves of test no. 3. a) Stress path in $p\prime$-τ space, b) Stress-strain curve, c) Pore pressure-strain curve.

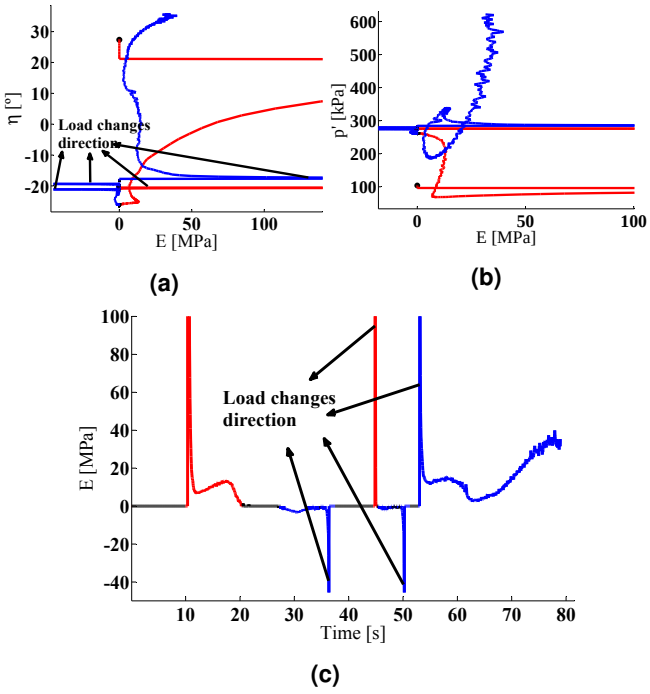

Figure 18. Stiffness curves of test no. 3. a) Stiffness distribution along the stress angle, b) Stiffness distribution along the mean stress, c) Stiffness timeseries.

Stiffness

Figure 18a shows the tangent stiffness distribution along the stress angle. Loading-down (red) starts from the top, with a spike of maximum stiffness and decreases with the angle going down. At the minimum angle plasticity is reached and here it can be seen that stiffness is not recovered until $\approx 5^o$ are lost. After this loading-up (blue) begins and negative tangent stiffness shows reaction force increasing while sample was still pulled apart. This is due to friction angle continuing to drop slightly further. When compressive displacement is applied a spike of positive stiffness appears indicating elasticity instant elastic region. As forced displacement continues into compression tangent stiffness approaches a value of ≈ 5 MPa at an angle of 12^o. Voids previously induced by extension close here rapidly. In cyclic loading this brief softening response, when voids induced during the opposite loading direction get closed, is the cause of liquefaction.

In Figure 18b an increase in stiffness between peaks can be observed along increasing hydrostatic axis. Zero stiffness is exhibited when stress state is moving down the hydrostatic axis.

From the timeseries in Figure 18c it can be seen that every time the loading is initiated or the loading direction changed there is a brief stiffness spike. In cases where loading direction is changed near the failure envelope a brief negative spike is noticed as resistance keeps decreasing even during compressing displacement increment is ongoing.

6. One-way cyclic loading

An increase in soil strength has been noticed during one-way undrained cyclic loading in compression or extension. During one-way cyclic loading the stiffness of the soil is also increasing. Moreover during this type of loading a completely new phenomena is detected: the pore pressure response vanishes changing completely the effective stress path followed by the soil. All these phenomenas are further investigated in this section.

6.1 Cyclic compression and followed after loading

The case in which this strengthning is most noticeable is when the load is significant enough to produce cavitation. Thus the behavior of a one-way cyclic loaded specimen in which the stress state is near initial maximum at the peak is investigated and described here.

Loading - Force control

This tests corresponds to the test number 15 in Table 1. This represents a critical case in which the load is large enough to produce cavitation. In this case the largest increase in soil strength has been observed.

In Figure 19a the timeseries of the force is shown in which it can be observed the cyclic loading and the post-cyclic loading. In Figure 19b the displacement timeseries of the test is shown and it is noticed that the displacements are stabilizing before failure in pure plastic softening regime.

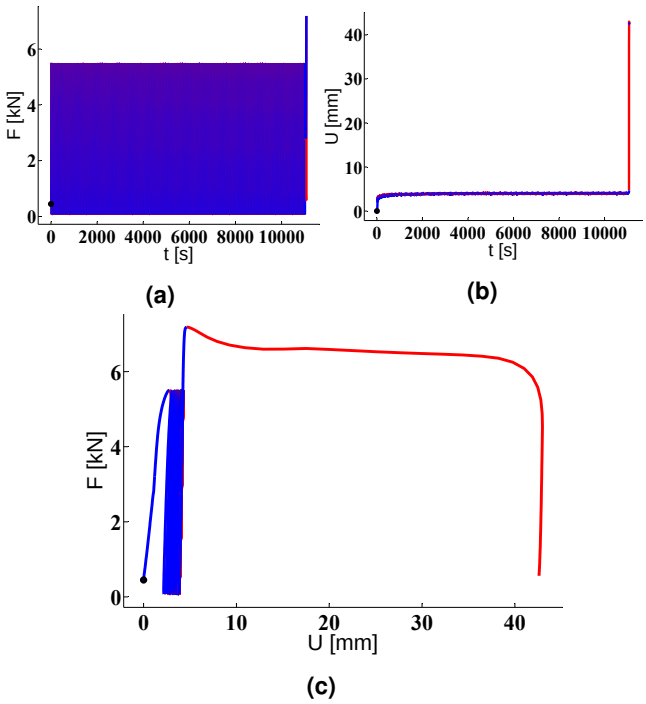

Figure 19. Loading and displacement curves of test no. 15. a) Force timeseries, b) displacement timeseries c)force-displacement curve.

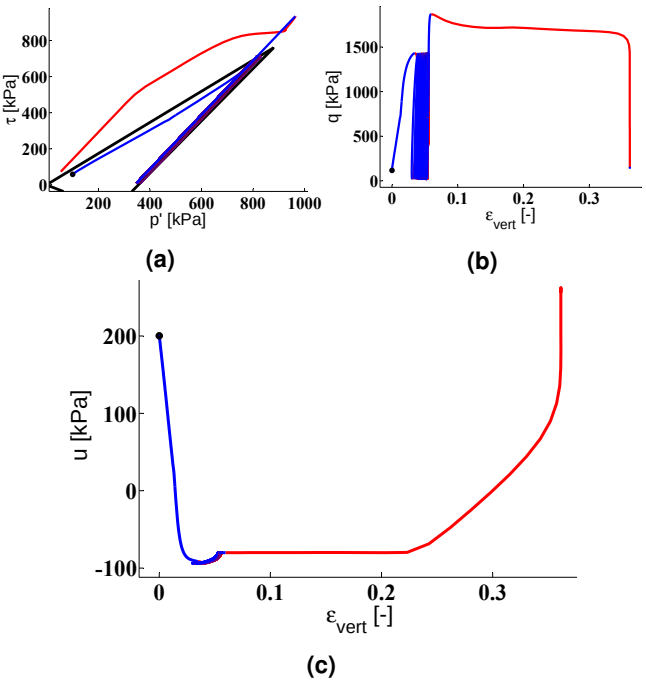

Figure 20. Stress and strain curves of test no. 15. a) Stress path in $p\prime$-τ space, b) Stress-strain curve, c) Pore pressure-strain curve.

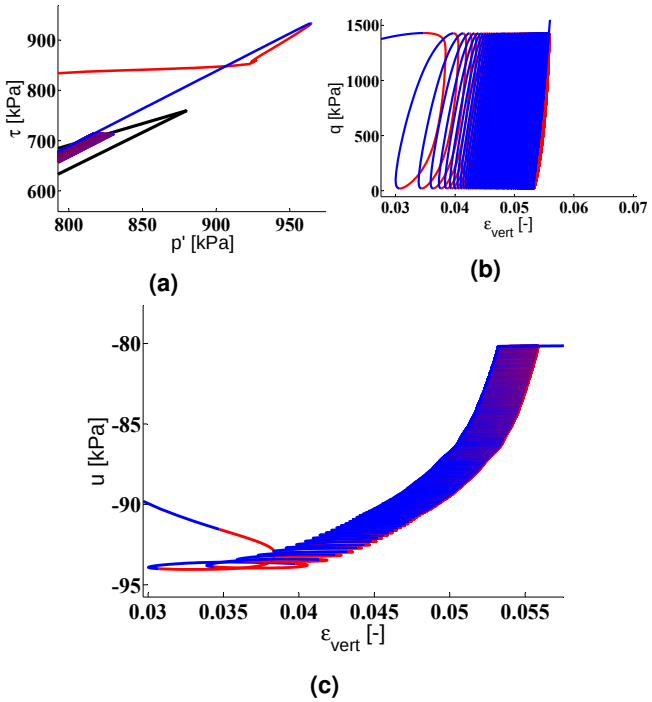

Figure 21. Stress and strain curves of test no. 15 close-up. a) Stress path in $p\prime$-τ space, b) Stress-strain curve, c) Pore pressure-strain curve.

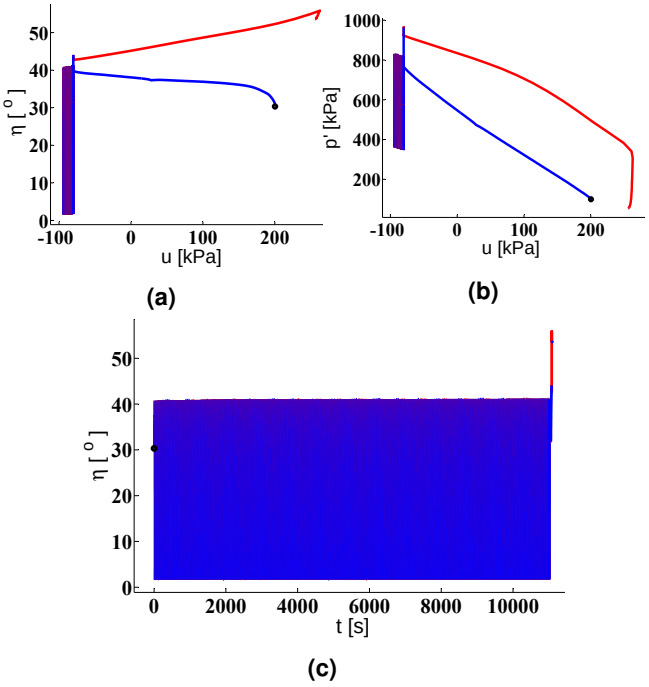

Figure 22. Pore pressure curves of test no. 15. a) Pore pressure distribution along stress angle, b) pore pressure distribution along mean effective stress, c) stress angle timeseries.

Less obvious to the observer's eye might be the reason behind the drop in reaction force in Figure 19c after the final load is applied. It is important to recognize that in this case the loading-down -blue line- is not done intentionally by the control system. It is the sample weakening and losing its reaction force, while the controller is trying to apply an even increasing force. Furthermore the increasing radius of the sample was not taken into account in the shear strength due to Poisson's ratio not being possible to measure in the cavitation regime, which should be somewhere in between the pure drained and undrained. If the increasing area was taken into account the stress capacity would be seen to continue dropping instead of staying rather horizontal through the plastic failure.

Stress and strain

The stress path induced in Mohr-Coulomb coordinate space can be seen in Figure 20a and a close up of the point where the failure envelope meets the $TSP + u_{cav}$ line is shown in Figure 21a. Looking at the close up it is visible how the cyclic stress develops slowly to the left crossing the initial envelope at some point. This does not trigger neither failure, nor a change in displacement development pattern as the failure envelope had already changed its position at that point in cyclic loading. When the final load is applied towards failure a new strength point is reached and this indicates that the friction angle has increased. In Figure 21b a zoom into Figure 20b is shown in which it can be noticed that the strain develops slower with further cyclic loading, meaning that the stiffness of the soil is increasing.

Density has been often used as the main factor determining the ultimate friction angle. An example function is shown in Equation 13 which was calibrated for Aalborg university sand no. 1 in [Ibsen et al., 2009].

$$\phi_t = 0.11 \cdot I_D + 32.3[^o] \tag{13}$$

$$c = 0.032 \cdot I_D + 3.52[kPa] \tag{14}$$

Density drops as voids increase while density increases as voids decrease. Figure 21c shows a tendency for increasing pore pressure in the cavitation zone which means that the voids reached during cavitation are gradually closing and density slightly increasing. Neither bulk modulus of the medium volume nor the Poisson's ratio is known precisely, thus measuring the exact volume change is not possible.

Density never goes beyond initial density but the undrained shear strength does increase beyond initial strength. This is thought to be due to increase in soil skeleton structure "efficiency".

During loading-down after failure, a stress state beyond the linear failure envelope is reached. Mohr-Coulomb models consider this state to be impossible, see [Helwany, 2007] and [Clausen and Damkilde, 2006]. It can be a consequence of deformations in the sample influencing the stress distribution area. Failure is reached at 40 mm which is more than half of the sample length. That should lead to a significant increase

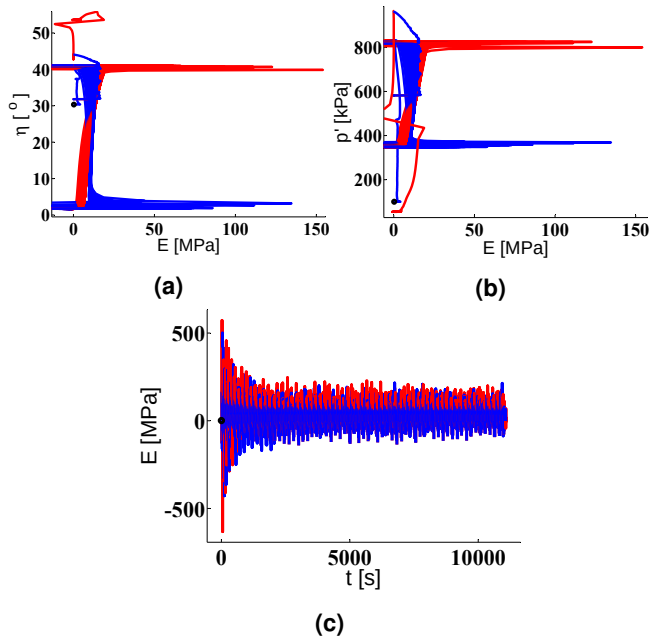

Figure 23. Stiffness curves of test no. 15. a) Stiffness distribution along the stress angle, b) Stiffness distribution along the mean stress, c) Stiffness timeseries.

of area that is providing the reaction force during the loading of the cylinder shaped sample, which is increasing in radius as the axial deformation is induced.

Volumetric strain in stress space

Looking at the influence of stress states to the volume change it is visible that the pore pressure increase is roughly linear along the hydrostatic axis, see Figure 22b, and is curving

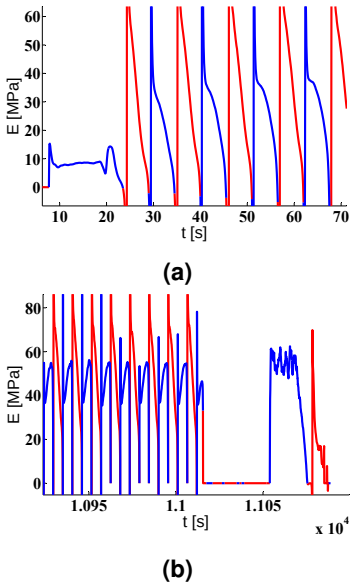

Figure 24. Stiffness curves of test no. 15 close-up.

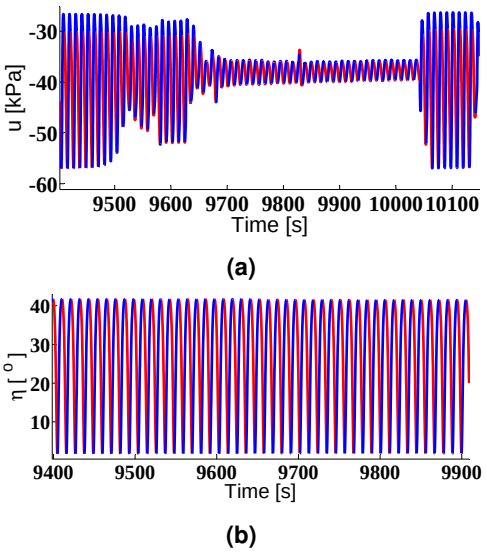

Figure 25. Observed transition of soil skeleton into a rock behaviour, test no. 14. a) Pore pressure timeseries, b) Stress angle timeseries.

towards being parallel during the first cycle. In Figure 22a it is observed a slightly increase in the stress angle after the cyclic loading. At failure the vertical stress reaction is gradually overestimated due to neglecting the increase in the area of the vertical plane of the specimen which is where the force is acting.

Stiffness

Stiffness distribution in Figure 23 indicates that a positive spike in stiffness is reached at the beginning of loading-up or loading-down. Right after a short negative stiffness indicating the displacement continues in plastic regime even though

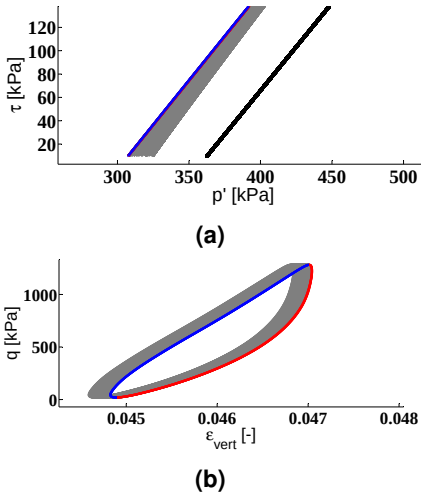

Figure 26. Observed transition of soil skeleton into a rock behaviour, test no. 14. a) Effective stress path, b) Stress-strain curve.

the load has changed direction, meaning that friction angle continues to drop and dilation still develops while the load is being decreased. At the beginning of the loading cycle the spikes of stiffness are bigger, see Figure 23a, while the average stiffness in between the peaks is growing with the number of cycles. This indicates the average stiffness to be increasing together with the density of the sample.

Distribution of the tangent stiffness modulus along the stress angle η exhibits a rather constant shape for loading-down, while loading-up (blue) path changes in shape from a tangent like Z-shape into a C-shape - spikes in stiffness develop when approaching the final stages of loading-up. The distributions are normalizing towards a stable shape where plastic deformations decrease and stabilize. Both stiffness paths have a similar shape along the hydrostatic axis after the state stabilizes, see Figure 23b with dilation decreasing the stiffness during loading-up path during the initial cycles much more than later on in the cyclic loading.

A close-up to the beggining of the stiffness timeseries in Figure 23c is shown in Figure 24a, while in Figure 24b it is noticed that the shape changes from one single peak in the first one to two peaks in the end part of the timeseries.

6.2 Cyclic compression - transition to rock behaviour

A transition zone of soil skeleton structure is observed in some tests. Figure 25a corresponds to the pore pressure timeseries of test no. 14 in Table 1. The transition is slightly complicated to observe in compression cyclic loading case. There is no influence in stress angle timeseries, see Figure 25b. The trajectory of effective stresses drifts very slightly away from TSP line angle, see Figure 26a. It will be shown that in extension is easier to detect this behaviour, in which the stress path shifts almost perpendicular to itself giving a very clear indication when the transition is complete or starts happening.

Transition is possible to see only if full cavitation has not occurred and the effective stress path was not locked-into the $TSP + u_{cav}$ path as shown in Figure 26a. The stress path is nearly parallel to the total stress path even though the pore pressure is far away from cavitation, see Figure 25a. If cavitation initiates then the pore pressure response is completely compromised by water vapor gas instead of a liquid stiffness. The transition state might be important as it gives an 'upper limit' of any further soil state development. The new state in which the pore pressure has no influence on the stress path of the soil does not influence in the stress-strain response of the soil as shown in Figure 26b.

6.3 Post-cyclic loading in compression restoring initial conditions after one-way cyclic compression

Now the test no. 13 in Table 1 is investigated. In this test the sample hold 1000 cycles and it was further loaded after restoring the initial K_0 conditions, meaning that the drainage valves were opened and the load was removed until K_0 conditions. Thus pore pressure returned to 200 kPa and the sample kept 'reset' to a drained K_0 state after the cyclic loading. Then the valves were closed again and an undrained monotonic load

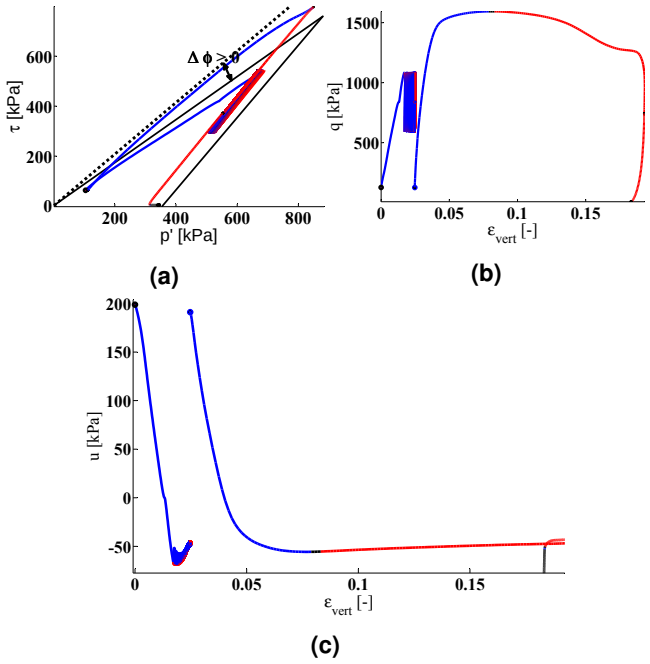

Figure 27. Stress and strain curves of test no. 13. a) Stress path in $p\prime$-τ space, b) Stress-strain curve, c) Pore pressure-strain curve.

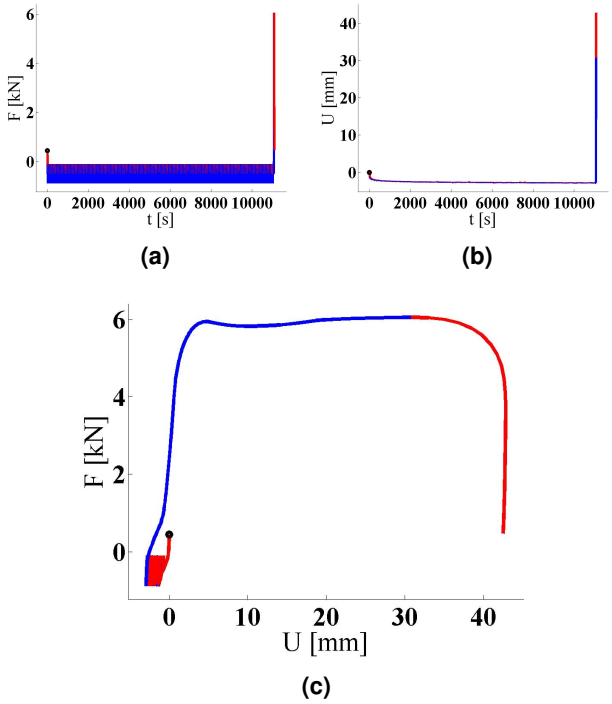

Figure 28. Loading and displacement curves of test no. 19. a) Force timeseries, b) displacement timeseries c)force-displacement curve.

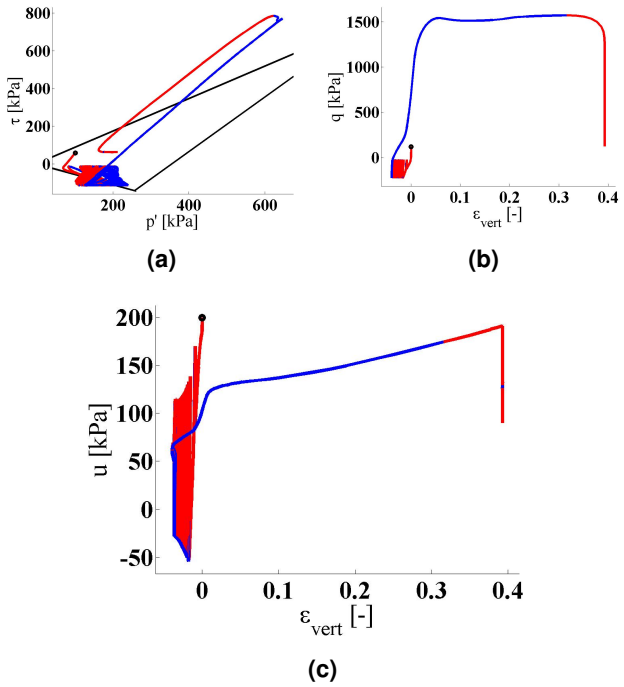

Figure 29. Stress and strain curves of test no. 19. a) Stress path in $p\prime$-τ space, b) Stress-strain curve, c) Pore pressure-strain curve.

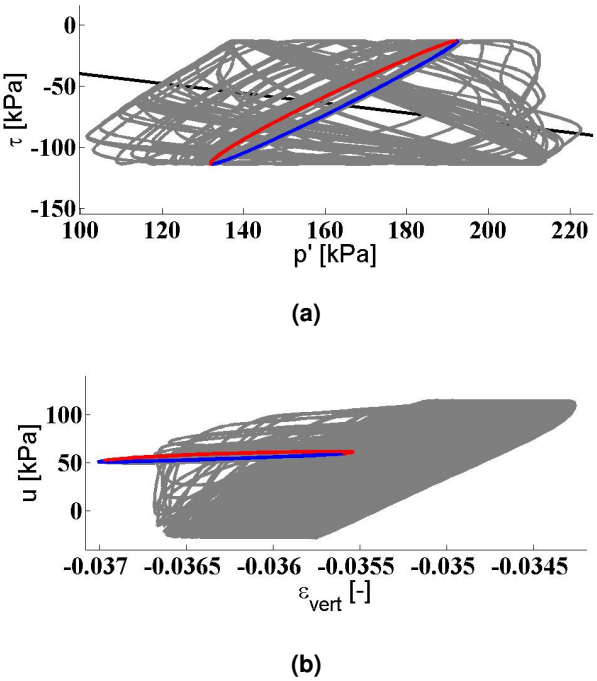

Figure 30. Observed transition of soil skeleton into a rock behaviour, test no. 19. a) Effective stress path, b) Pore pressure-strain curve.

was applied until failure. The resulting stress path clearly shows a drift along an increased friction envelope and can be seen in Figure 27a. The angle of the new envelope is close to 45 ^{o} while initially it was close to 42 ^{o}.

6.4 Cyclic extension followed by after loading in compression

Extension one-way cyclic loading in undrained conditions exhibits some very interesting behaviours. In this regime of loading the exchange between increasing and decreasing failure envelope angle can be observed in a unstable stress path transitional regime, as it will be explained and illustrated later on. The exact mechanism behind it and complete set of properties have not been found yet, but the turbulent transition zone is consistently repeating itself under similar loading conditions in multiple tests.

Loading - Force control

This test corresponds to the test no. 19 of the series presented in Table 1. In this test force control was used. The force timeseries is shown in Figure 28a. A compression to failure load was applied after 1000 cycles. The post-cyclic strength reached is about 7 % larger than the initial one.

In Figure 28 the loading and displacement curves are illustrated in which it can be seen that the after loading is performed in compression.

Stress and strain

The stress path in Mohr-Coulomb coordinates is shown in Figure 29a. It might look messy at first glimpse. An illustration of before and after transformation stable stress paths mentioned before is plotted in Figure 30a. Looking at the directions of stress path it looks like the initial one is heavily based on dilation and contraction, while after transition the path looks more like an elastic stress path.

The sequence of developing in transition follows this points:

1. During loading-up (blue line) the sample hardens while contracting.

2. During loading-down (pulling the sample) the envelope is reached slightly later than previous cycles did. Dilation is initiated and as the load progresses the envelope keeps softening.

3. During loading-up again the sample hardens and pushes the envelope

This struggle of softening and hardening creates the clutter in the transition zone, see Figure 29 while further away from the unstable state the stress paths are very stable and clearly distinguishable.

The new post-transitional state of the soil is neither contracting nor dilating. It seems to exhibit a much higher friction angle but the stress path looks more like drained. When the

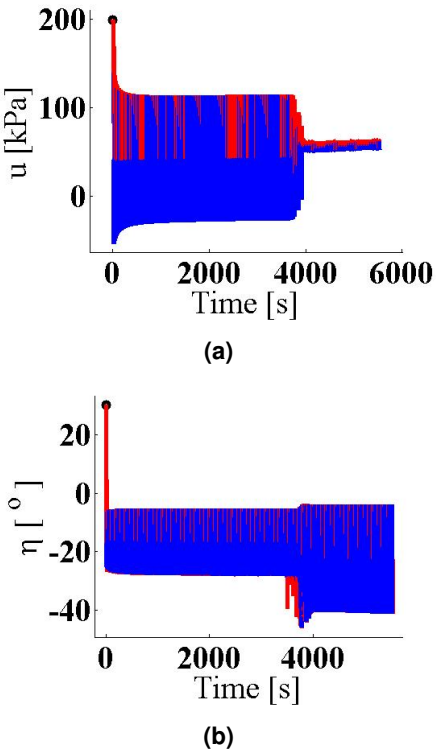

Figure 31. Observed transition of soil skeleton into a rock behaviour, test no. 19. a) Pore pressure timeseries, b) Stress angle timeseries.

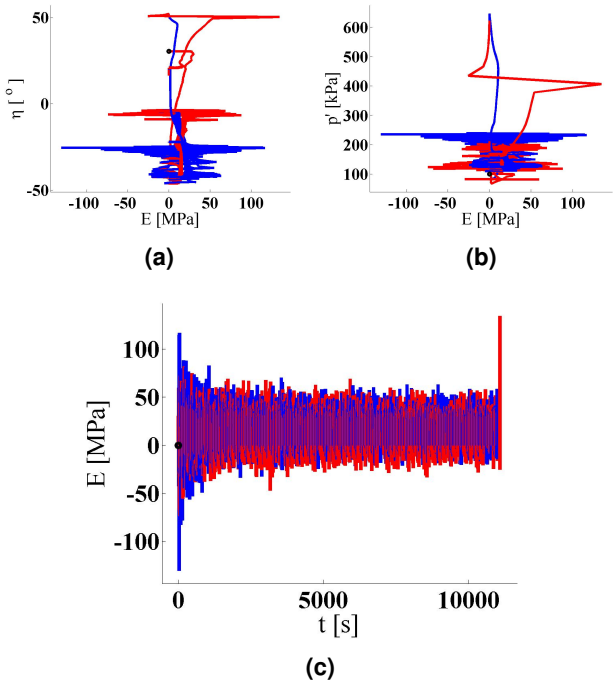

Figure 32. Stiffness curves of test no. 19. a) Stiffness distribution along the stress angle, b) Stiffness distribution along the mean stress, c) Stiffness timeseries.

increased shear angle is reached the sample collapses gradually, with no dilation, as seen in Figure 29c and the close-up in Figure 30b.

One of the observations so far is that the state is not density driven. It does not dilate further nor does it liquefy. Rather it seems it is the particle distribution in the sample that has rearranged. The friction angle did change significantly, but without much of a volume change. This indicates a more "efficient" stress distribution was reached maintaining the same void volume in soil. Even though the transition looks chaotic and complicated, the displacement response does not seem to be influenced by it too much, i.e., the vertical strain continues stabilizing.

Volumetric strain in stress space

It was shown in the cyclic compression that the stress path changes completely being parallel to the total stress path meaning that the pore pressure response vanishes. A closeup of the transition of the pore pressure response is given in Figure 31a. While the sample stress state is sliding back and forth near the failure envelope a relatively large amplitude of pore pressure response is noticeable, while after sample goes through the transformation the amplitude of response becomes close to zero. The stress angle amplitude on the other hand enlarges after the transition, see Figure 31b.

Stiffness

Due to big changes happening in terms of the shear angle, the tangent stiffness plots in Figure 32 look quite messy. If this is analyzed in detail, questions arises regarding to modeling techniques that use Terzaghi-based effective stress approximation. When plotting the sequence in an animation it becomes visible how the average stiffness of the system is increasing with each loading cycle. At some point the stress angle starts to vacillate and its lower values drop rather arbitrary. It can be postulated that this phenomenom is due to stiffness of skeleton increasing. Here the effective stress approximation by Terzaghi, see Equation 15, might be replaced by Biot approximation in Equation 16, where the bulk modulus ratio between skeleton and particle is taken into account, see [Yangsheng et al., 2003]. If $\alpha = (1 - K_{rock}/K_{grain})$ approaches values closer to zero then pore pressure response vanishes. Thus sand begins acting like a porous rock.

$$\sigma' = \sigma_{tot} - u \tag{15}$$

$$\sigma' = \sigma_{tot} - \alpha u \tag{16}$$

6.5 Cyclic extension and after loading in extension

The previous test was repeated, and the transition zone was again obtained. In this case there was not a complete change of the stress path and the pore pressure did not finally converge after the turbulent transition. In this case the sample was after-loaded in extension and a slightly smaller strength was

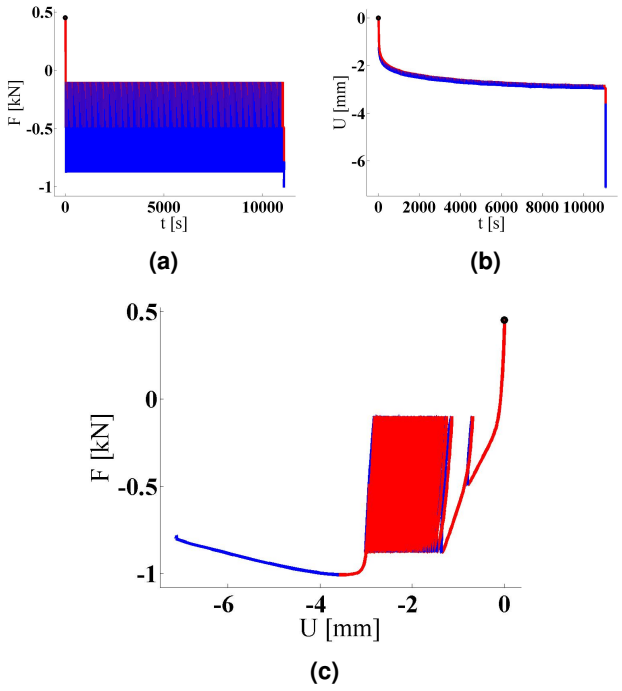

Figure 33. Loading and displacement curves of test no. 20. a) Force timeseries, b) displacement timeseries c)force-displacement curve.

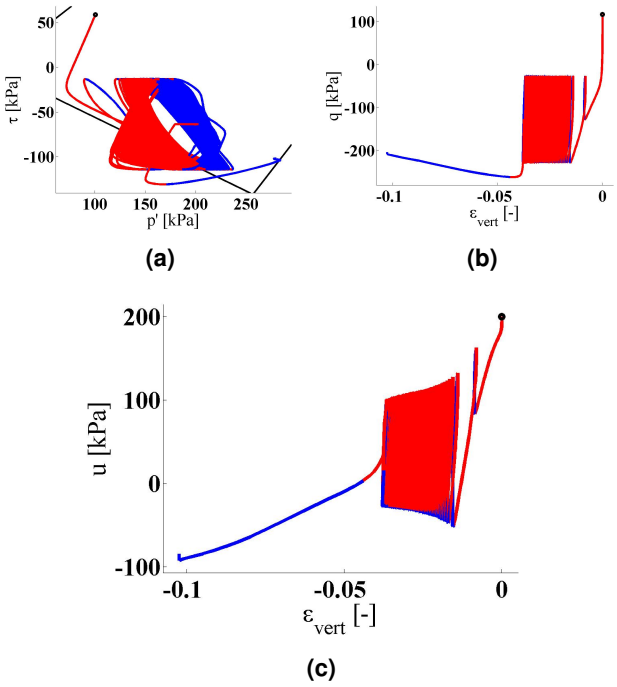

Figure 34. Stress and strain curves of test no. 20. a) Stress path in $p\prime$-τ space, b) Stress-strain curve, c) Pore pressure-strain curve.

reached. The test corresponds to the no. 20 of the series in Table 1. Instances when converging appeared give a small rise in cycle stiffness and if it failed to converge a slight drop in cyclic stiffness was visible, see [Troya et al., 2014] for the definition of cyclic stiffness. This transition part was also noticed in compression tests, though much less visible in the principle stress space, but clearly noticeable in pore pressure response history.

In Figure 33 load induced displacements are seen to normalize to a near stable state of displacement, while the stress path in Figure 34a are a lot less stable.

Even though the pore pressure did not converge into a stable value completely, there was still a rather gradual drop in pore pressure which suggests little to no 'density' being left to induce dilation while the pore pressure is dropping because of the sample being pulled apart. Just like it would happen in an elastic body with a Poisson's ratio below 0.5. Interestingly enough that at cavitation the stress state bumps into the $TSP + u_{cav}$ line and stays there.

Abnormal trajectory of the stress-strain curve is seen in Figure 34b where the loading-down goes through the initial failure envelope, then sharply turns away as if dilating for a moment, and keeps dropping. In practice the drop might not be that steep as diameter of the sample is contracting and the reaction load is distributed over a decreasing area.

The plots in Figure 34 show the clutter along angle and mean effective stress. This is a consequence of sample not being able to find the equilibrium condition. The extreme

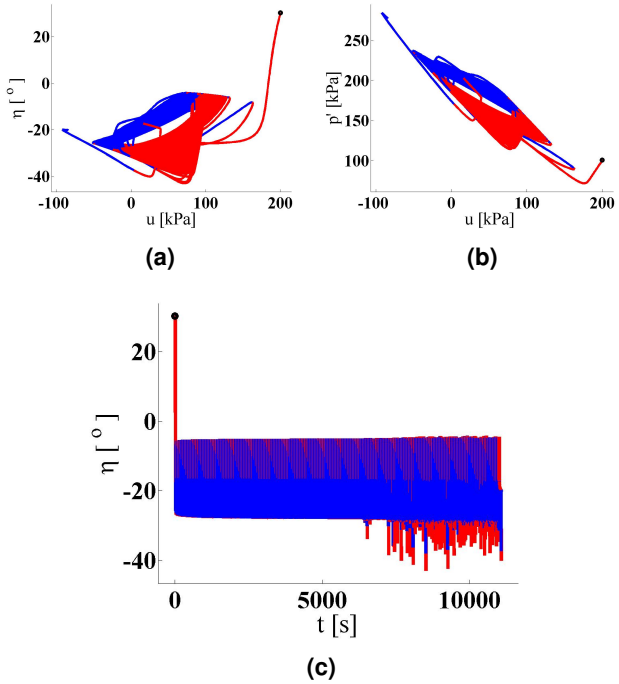

Figure 35. Pore pressure curves of test no. 20. a) Pore pressure distribution along stress angle, b) pore pressure distribution along mean effective stress, c) stress angle timeseries.

down-crossings in Figure 35c show clear indications where the transition had spikes of transforming, that never completely converged.

The transition state gives an 'upper limit' of any further soil state development. The sample does not dilate or contract further on unless the new structure is disturbed. It looks like a porous, permeable rock.

The pore pressure towards which transformation converges indicates the final void state of the specimen. It is 50 kPa for extension and −40 kPa for compression cyclic loading induced transformation. This indicates that after the transformation a constant void level is fixed.

It is not clear if the voids adopt in accordance with the induced deformation or if the state is induced due to applied stresses. Extension and compression have two very different stress states being dominant. Looking closer into this state might potentially reveal the exact solution of return mapping and stress state propagation rules for modeling plastic and elasto-plastic soil response in FEM.

7. Cyclic two-way loading

Two-way loading leads to degradation of soil strength. Liquefaction is common in two-way loading, even for 90 % relative density sand. This happens when the cyclic stress path crosses the 0 shear stress line.

If the load is dominated by one-way loading then full liquefaction will be prevented, stiffness will still increase but the friction angle will still decrease. Even though liquefaction does not develop to full extent, the small amount of two-way loading can cause failure by incremental collapse, see [Troya et al., 2014].

If the load is dominated by two-way loading then liquefaction will not be prevented. Excess pore pressure will acumulate, stiffness will drop and the friction angle will gradually drop to a value that will induce cavitation and failure will occur.

"Efficiency" of the microstructure of the soil is lost during any form of two-way loading. Observed patterns indicate that one-way loading is mandatory for efficiency to increase, while even the slightest crossing over the 0 shear stress line results in some amount of weakening in the soil.

Separate stages of the development in the plots will be introduced to aid in seeing the patterns. It is challenging to describe something made up of 1000 cycles plotted on top of each other and an animated explanation would be highly beneficial in this case. A good approach to make sense of it all is to follow the time plots for guidance and try to narrow down on the patterns within the same range in the next plot.

7.1 Symmetric two-way loading

In this type of loading it is observed an asymmetric developed displacement towards extension, which is due to the factor that the Mohr-Coulomb envelope is asymmetric, see [Praastrup et al., 1999] and [Ibsen and Praastrup, 2002]. Failure of

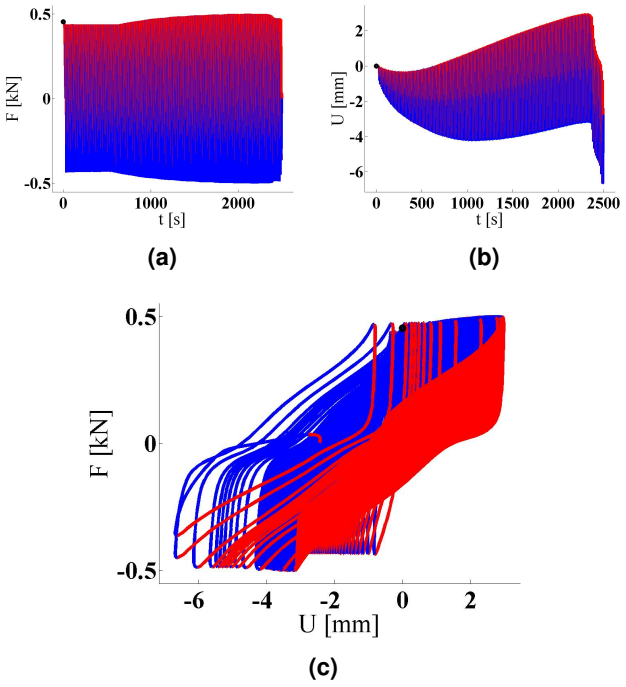

Figure 36. Loading and displacement curves of test no. 22. a) Force timeseries, b) displacement timeseries c)force-displacement curve.

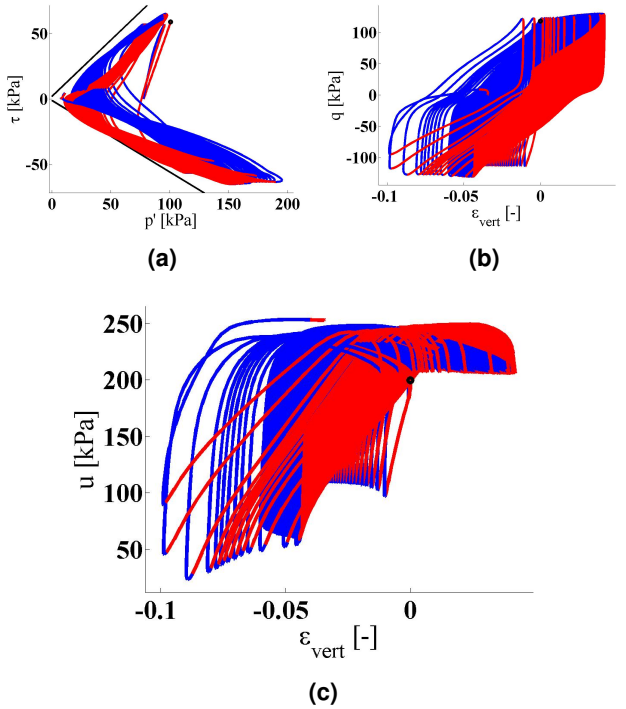

Figure 37. Stress and strain curves of test no. 22. a) Stress path in $p\prime$-τ space, b) Stress-strain curve, c) Pore pressure-strain curve.

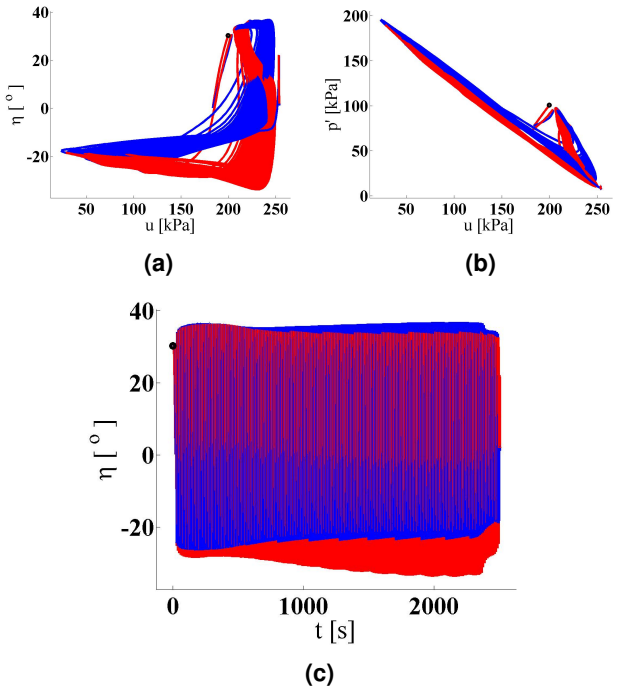

Figure 38. Pore pressure curves of test no. 22. a) Pore pressure distribution along stress angle, b) pore pressure distribution along mean effective stress, c) stress angle timeseries.

the sample is driven by liquefaction phenomena, due to a weakening of the soil and a loss of stiffness.

Loading - Force control

This test corresponds to the test no. 22 in Table 1. Loading was applied force controlled around the average of 0. A slight increase in amplitude is noticeable as the loading progresses, see Figure 36a. Looking at the displacements timeseries in 36b it is noticed how the mean value of resultant displacements initially lowers down, then raises up and then finally fails in extension again. The amplitude of the displacements is gradually increasing as stiffness is decreasing during the common stress path (CSP), see [Nielsen et al., 2013], next to the failure envelope. The next cycle brings less dilation, and slightly more contraction. In Figure 36c it can be seen the previous mentioned asymmetric displacements towards extension.

Stress and strain

In Figure 37a the stress path starts from climbing along the failure surface, while gradually dropping along the stress angle. First loading-down follows the ratio of $2/3$ and as the loading progresses the stress path goes further down the hydrostatic axis towards 0 mean effective stress. While decreasing confining stress it also extends its path along the failure envelope and therefore the amplitude of plastic deformations keeps growing proportional to it.

Strain is increasing in amplitude, initially moving the

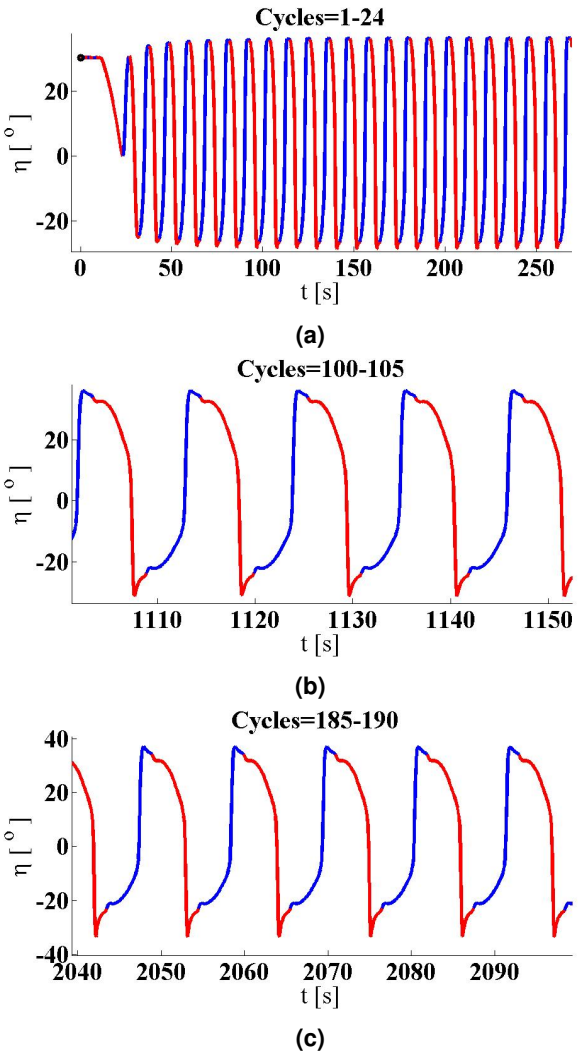

Figure 39. Close-up to the stress angle timeseries of test no. 22.

average towards failure in extension, then recovering with the average moving towards compression and finaly failing due to liquefaction in extension, see Figure 37b. In Figure 37c it is visible that complete cavitation is never reached through the cycles, and dilation becomes more sensitive to the shear stress increment.

Volumetric strain in stress space

Two-way loading decreases soil skeleton efficiency. This leads to gradually increasing dilation sensitivity to shear stress changes and a very noticeable drop of friction angle along the cycles.

Figure 38a shows how the pore pressure at the peaks approaches closer to 250 kPa while the mean effective stress comes near 10 kPa short of complete liquefaction. Dilation increase is slightly less noticeable, but still present. Dilation takes an even increasing amount of friction angle away from the sample, as can be seen from the red area. Even though

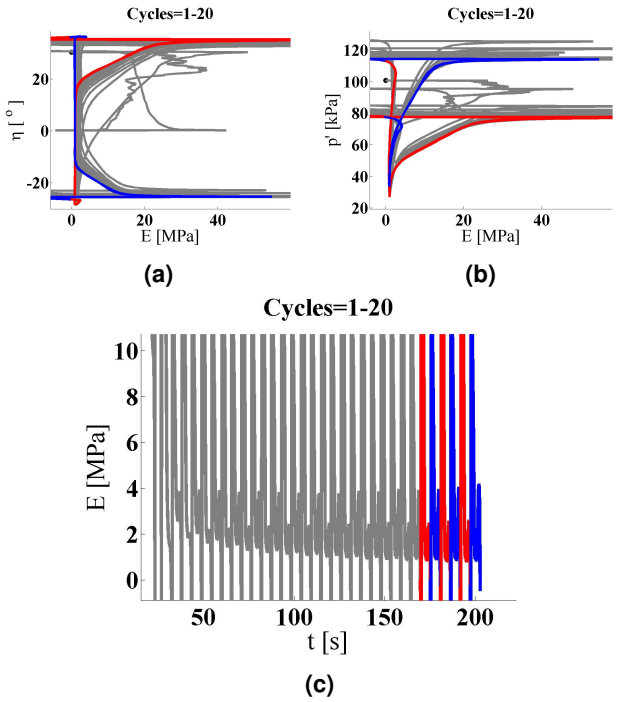

Figure 40. Stiffness curves (1) of test no. 22. a) Stiffness distribution along the stress angle, b) Stiffness distribution along the mean stress, c) Stiffness timeseries.

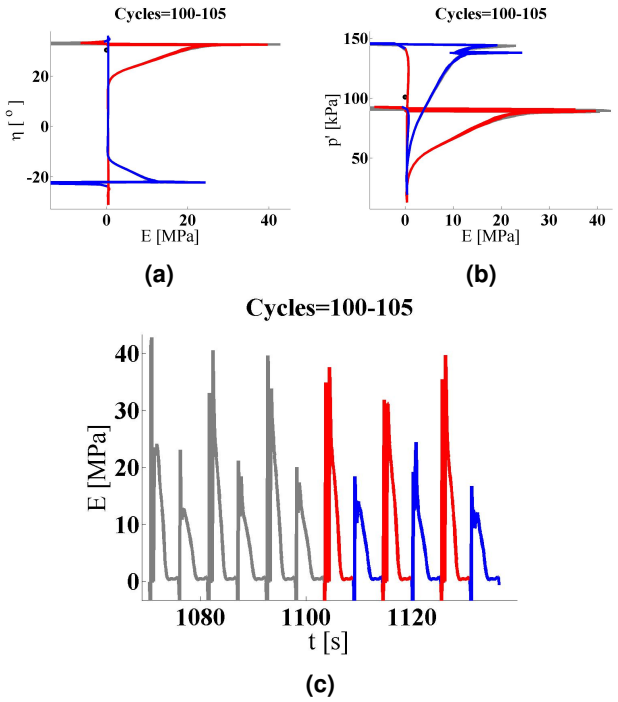

Figure 41. Stiffness curves (2) of test no. 22. a) Stiffness distribution along the stress angle, b) Stiffness distribution along the mean stress, c) Stiffness timeseries.

there is a small increase in loading amplitude due to MOOG system trying to catch up with the softening of the sample, the drop in friction angle accommodating the reduction in stiffness is very much noticeable.

Figure 38c shows the timeseries of shear angle, in which it can be seen the distribution of the shear angle loss. The red plot dominating in the bottom part of the timeseries, and the slight blue in the top of the peaks illustrate how much the stress angle drops, before an elastic reaction is reached. The gap between the CSP line and return to elastic reaction keeps increasing with loss of efficiency. Unlike the common practice of returning to elastic response as soon as the load changes direction measurements indicate there is up to 10 ^{o} drop in friction angle as the sample is being unloaded. This is often simulated by a curved MC model, but this curvature is not present through initial stages. Fitting one variable of a linear model with a dropping/recovering friction angle might be a more efficient option than trying to fit multi-parameter curved MC envelope thorough the loading sequence.

Figure 39 shows a close up view of how the angle response changes during liquefaction of very dense sand. Initial cycles in Figure 39a can be seen to follow the sinusoidal loading rather precisely. With a small stress angle drop being developed in the negative peaks as early as the second load cycle. The friction angle gradually increasing towards larger extremes during the initial loading cycles. Then Figure 39b shows a steady shape of resulting stress angle with loads. The angle can be seen to drop slightly in final stages of each

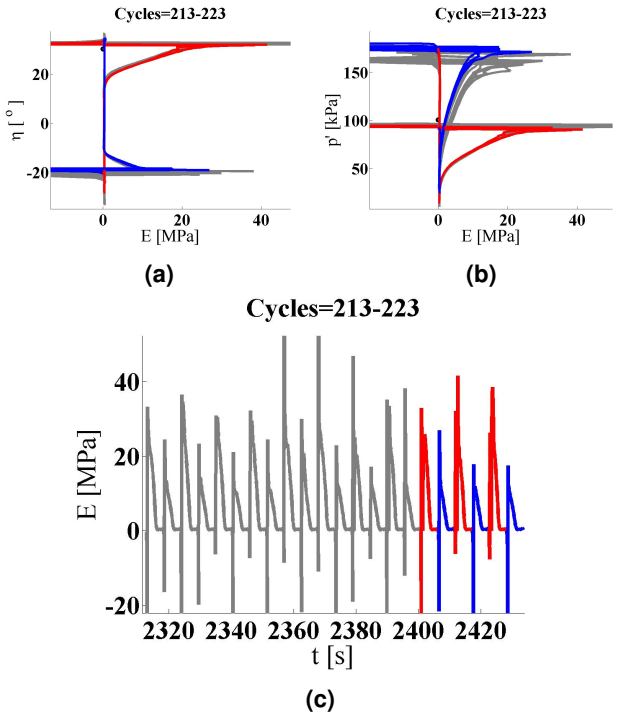

Figure 42. Stiffness curves (3)of test no. 22. a) Stiffness distribution along the stress angle, b) Stiffness distribution along the mean stress, c) Stiffness timeseries.

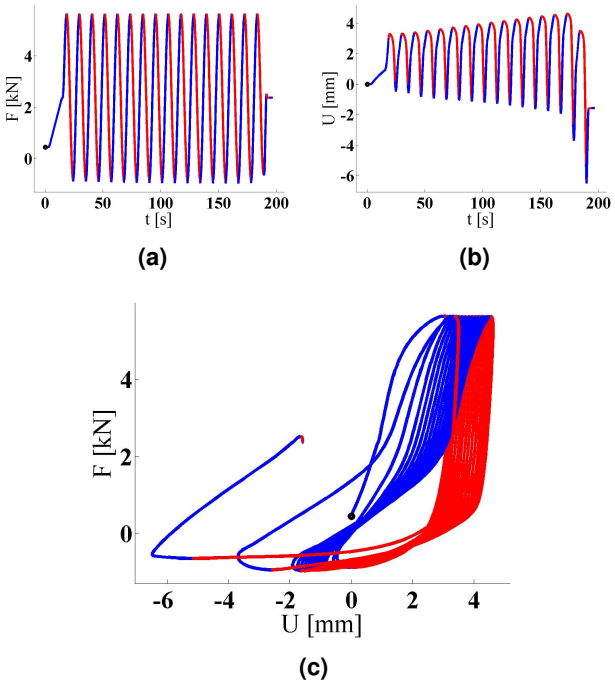

Figure 43. Loading and displacement curves of test no. 21. a) Force timeseries, b) displacement timeseries c)force-displacement curve.

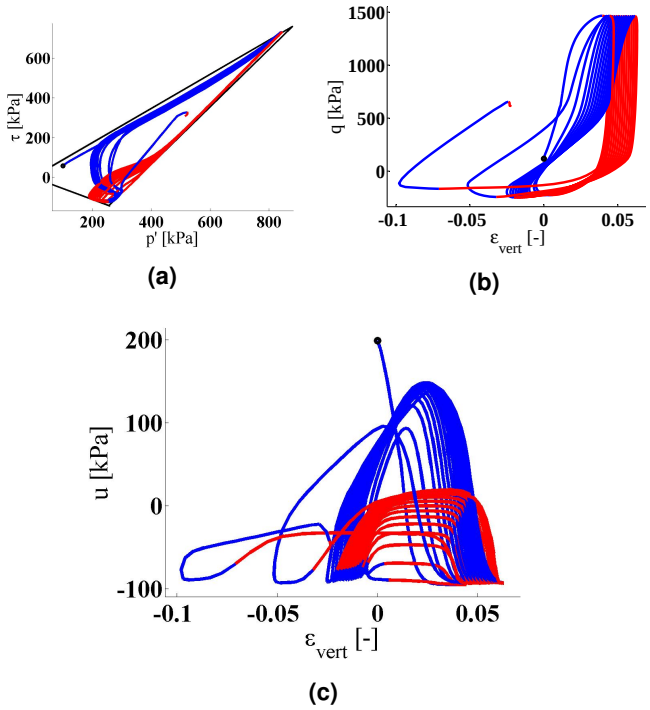

Figure 44. Stress and strain curves of test no. 21. a) Stress path in $p\prime$-τ space, b) Stress-strain curve, c) Pore pressure-strain curve.

loading-up and 'bump' into the stable failure envelope during initial stages of loading-down. In numerical models a steady value of an angle indicates an associated flow rule to be followed at that exact angle through time. The same pattern is followed in the bottom part, with a sharper stress angle drop. The last cycles before liquefaction failure in extension are shown in Figure 39c. The angle can be seen to reach smaller amplitude in the negative side of the stresses, explained by underestimating true stresses due to loss of reaction area in extension through Poisson's ratio.

Stiffness

Stiffness is gradually lost. During the first cycles shown in Figure 40 half of the transitional stiffness is lost during last parts of a loading phase, before loading direction is changed. Peak stiffness which occurs right after a loading direction changes and elastic regime is reached remains rather constant. Stiffness transition angle during loading-down changes rapidly with each cycle from $-20\,^o$ to $0\,^o$ of stress angle and slows down from $10\,^o$ and up.

A pattern of two peeks can be observed right after shift in direction in the middle of liquefaction. The spike before the change of direction is gone. Stiffness transition value during loading-down starts at $\approx 16\,^o$, see Figure 41.

By the end of the cycles the two peak mode dissipates. Stiffness transition value during loading-down starts at $\approx 18\,^o$ as shown in Figure 42.

7.2 Peak-to-peak two-way loading

A cyclic loading case, where the load applied goes from one limit state to the other, from maximum to minimum shear strength and back, inducing cavitation in both extremes on the edge of failure is investigated in this section. This is interesting, as it cover the whole plausible amplitude, being a limit state of possible to apply amplitude.

Loading - Force control

Figure 43 shows the dense sand soil response to force controlled loading of maximum amplitude. A rather symmetric and linear increase in induced displacement amplitude can be seen in Figure 43b. In Figure 43c all three phases of elastic, elasto-plastic and pure elastic response are distinguishable in the loading-down (red) part of the response.

Stress and strain

Figure 44a shows the effective stress path in MC coordinates. Development of the stresses start by following loading-up path parallel along the failure envelope, cavitating in the up- and down-scaling through the $TSP + u_{cav}$ line without any measurable contraction. In the next cycles contraction becomes increasingly more noticeable, ant starts earlier on in loading-down. Figure 44b shows the distribution of plastic strains. It is interesting to notice how stiffness is not lost in the upper part of positive loading. This is in contrast with the symmetric stress path resulting from a a symmetric two-way loading, see 37b.

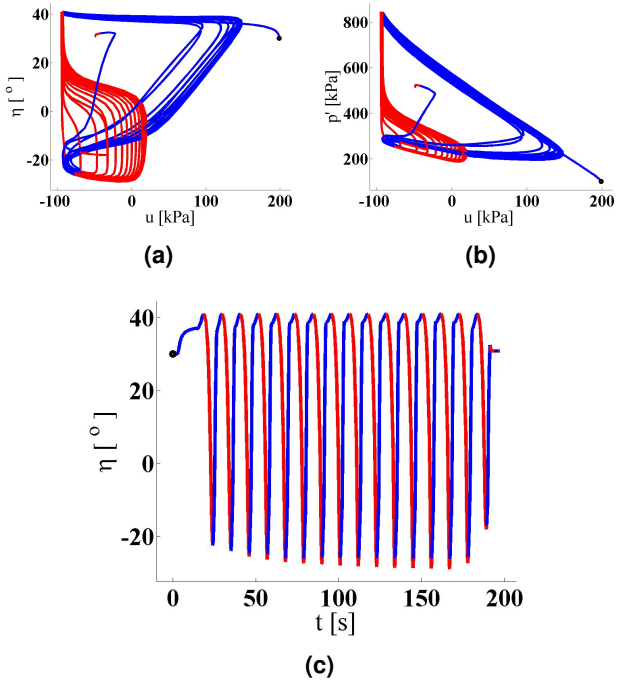

Figure 45. Pore pressure curves of test no. 21. a) Pore pressure distribution along stress angle, b) pore pressure distribution along mean effective stress, c) stress angle timeseries.

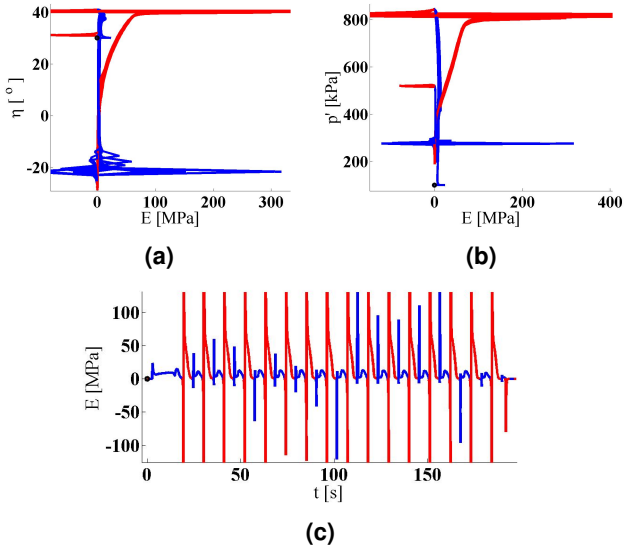

Figure 46. Stiffness curves of test no. 21. a) Stiffness distribution along the stress angle, b) Stiffness distribution along the mean stress, c) Stiffness timeseries.

In Figure 44c it is visible how cavitation is induced and maintained through strain amplitude development. With increasing amplitude the voids keep closing more, though never until complete liquefaction, as the maximum pore pressure is always below the initial level, 200 kPa.

Volumetric strain in stress space

Contractile properties can be seen to grow in a logarithmic manner with each loading-down and loading-up along the angle in Figure 45a. The shapes are rather constant and support the Prevost approach, see [Yang et al., 2003], where the shapes are fitted with shapes provided by Equations 11 and 12. During dilation the stress angle is rather constant, confirming a linear MC associated flow rule is very well suited for this case, no significant curvature is exhibited on the stress path.

Figure 45c shows how stress angle is distributed by a sinusoidal, peak to peak load. In compression a longer lasting 'lock-in' of the angle is visible, as the stress path along the failure envelope in compression a lot longer. Interestingly in this case there is almost no friction angle drop. Only a very slight, $1\ ^o$ or $2\ ^o$ angle drop in peak extension develops during loading-down.

Stiffness

Figures 46a and 46b show an noticeable difference in the amount the stiffness spreads. In this case it can be observed how much more the loading-down stress paths overlap when plotted along the hydrostatic axis. During loading-up Figure 46 plots show a lot of softening in the end of loading-up path. Judging by the timeseries in the bottom of the plot, it seems like the stiffness is initially increasing and then dropping while still following the CSP. This is the exact opposite tendency to the symmetric pre-cavitation two way loading, where this second 'bump' has completely dissipated before liquefaction, comparing Figures 46c and 42c.

This completes the different responses found in different cases of stress paths. If a material model is used for cyclic loading on dense sand, it has to capture those individual behaviours or at least the loading peak values with some amount of conservative approximation.

8. Mobilisation space explicit model

During experimentation an increasing complexity of responses was found. This behaviour seems to follow a rather simple set of rules in total stress space. A total stress response based model can be calibrated to capture most of the response without adding extra variables to the approximation.

A Maxwell type material model with rate independent damper can be used, see Figure 47, similar to the rate independent damping Kelvin model described in [Ishihara, 1996]. This model is tuned to capture the observed stress to strain path development. It does not use the exact effective stresses state history like Prevost [Yang et al., 2003] or other [LeBlanc et al., 2008] multi-surface models. Instead suggesting a much more explicit, TSP-based approach that is fitted directly on test data and can be scaled in accordance with τ_f^{max} and τ_f^{min}.

The model uses a static MC envelope to obtain τ_f^{max} and τ_f^{min} to normalize towards the total mobilization response, $-1 < Mob < 1$. A cylinder-like surface is following the stress

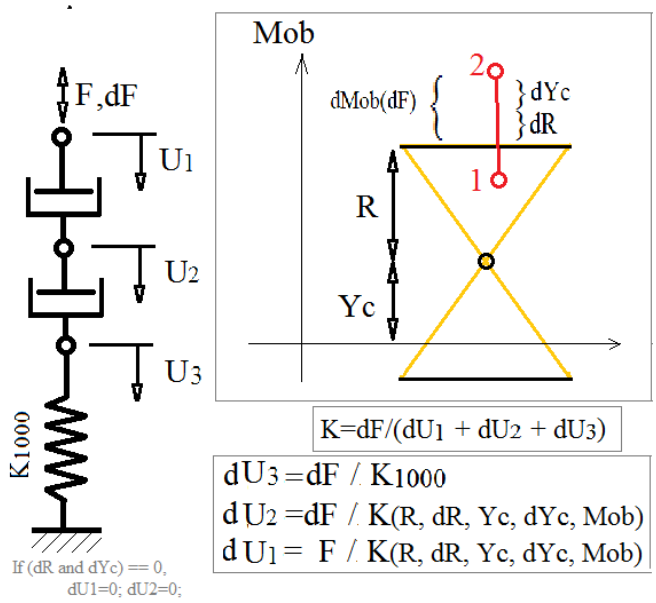

Figure 47. Sketch of Maxwell type material model

state, as illustrated in Figure 48. Each time a stress goes over the edge of the internal surface the radius of the cylinder changes and its center of coordinates moves. Both kinematic and isotropic hardening properties are present in the internal yield surface. MC envelope is used only to normalize the shear stress values and plays no further role, i.e., no stress return mapping required. Here the maximum and minimum shear stress from Equations 3 and 4 determines if the stress state is valid or not.

The necessity for going into Mob-space, see Figure 3 to distinguish between M and Mob, was observed when in peak to peak loading gave a symmetrical increase in displacement amplitude. Thus loading from -1 to 1 values of M gives a symmetrical response even though it corresponds to -134 to 735 kPa shear stress amplitude. Loading with a symmetrical value around a zero stress state gives a one-way increase in displacement amplitude. Transforming the stress state into the Mob space allows to capture this uneven distribution of strain reaction, by making strain a function of Mob rather than of stress.

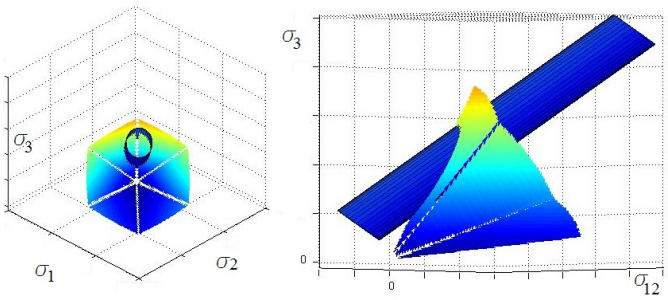

Figure 48. Illustration of the proposed model in principle stress space.

In the model proposed the internal failure envelope depends on 2 parameters: Radius, R, and its center of coordinates, Y_c, see Figure 47. Inside the space between the limits $Y_c + R$ and $Y_c - R$, the response is pure elastic. It could be made into a hysteresis loop but the curvature is small. Thus a line was found to be appropriate. While the stress state is inside the elastic area there are no plastic deformations occurring.

When a stress crosses one of the borders of the surface R changes and a transition displacement of Y_c occurs, dragging the edge closer to the stress state, compensating for the excess Mob. The proportion between dY_c and dR can be varied. Higher percent compensated towards hardening will give faster hardening and smaller hysteresis loop amplitude. Dedicating more to dY_c will give less hardening. In case the coefficients are chosen so that $[dY_c + dR < dMob]$, the envelope will take more than one step to catch up to the stress state, leading to simulation of creep. This is found quite advantageous as it allows to model the creep effect present in testing at frequencies of 0.1 Hz. Finally, leaving the envelope to not completely reach the stress state shot also makes the curves smooth.

The factor influencing dR and dY_c were made to fulfil the following rules:

1. If $(dMob * Mob) > 0$ then $dR >> 0$; Radius increases rapidly when loading past the previous maximum
2. If $(dMob * Mob) < 0$ then $dR \approx 0$; during loading-down towards 0, radius is stable.
3. $\text{sign}(dMob) = \text{sign}(dY_c)$; Which ever limit is passed, the surface center moves proportionally towards that stress state.
4. If $(Y_c * Mob) < 0$ then $dR << 0$; if the center of the hardening surface is on the other side of the Mob space than the currently active stress state, radius R is dropping rapidly and softening the soil, by inducing excess plastic deformation.

Each of the components in Figure 47 had a seperate flow rule attached to it with a unique purpose:

- U_1 - a plastic displacement is activated by $\text{sign}(Mob * dMob) > 0$. This is activated when the surface facing towards the failure envelope is crossed, activating a plastic reaction equal to that as if the part was loaded for the first time. If this was run alone it would emulate the unloading/reloading progression without a hysteresis loop.
- U_2 - a plastic displacement that forms the hysteresis loops contours. It is obtained by dividing dF. If run alone, this should provide a shrinking or increasing hysteresis loop that is not propagating too far forward or backward. The hysteresis loop of $U2$ needs to be pushed forth and back by U_1.

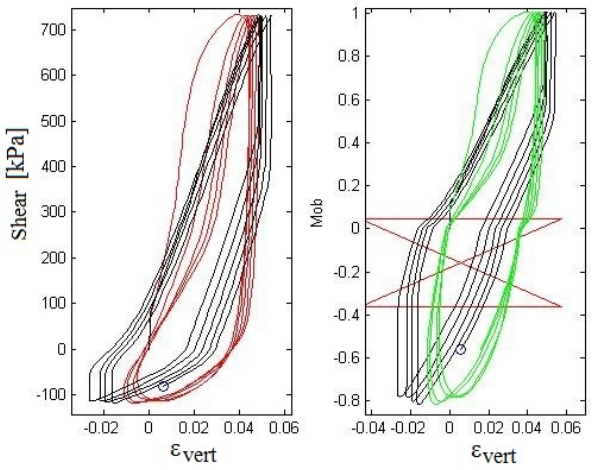

Figure 49. Peak-to-peak simulation of explicit TSP-based model proposed.

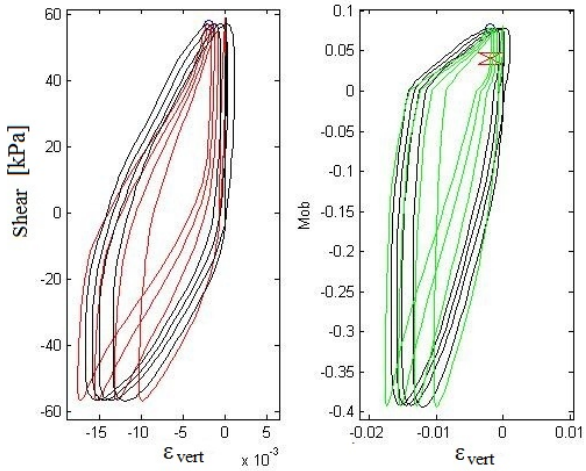

Figure 51. Symmetric two-way loading simulation of explicit TSP-based model proposed.

- U_3 - Elastc spring. When no yielding is present, inside the elastic region. It also tilts the hysteresis loops slightly.

A way of fine tuning the model has not yet been completely established. It is unclear how well it would perform with multiple elements. There is a tendency to have infinite displacements due to very small stiffness developing in two-way loading, but in a system of elements that should not be a problem. It rather allows to emulate liquefaction.

The possibility of using τ_{uf} as a scaling factor for the design diagrams introduced in [Nielsen et al., 2013] and [Troya et al., 2014] is extended with this model. So far results of model simulations presented in Figures 49, 50 and 51 indicate a possibility of using explicit TSP-based approximations to simulate the real behaviour of dense sand.

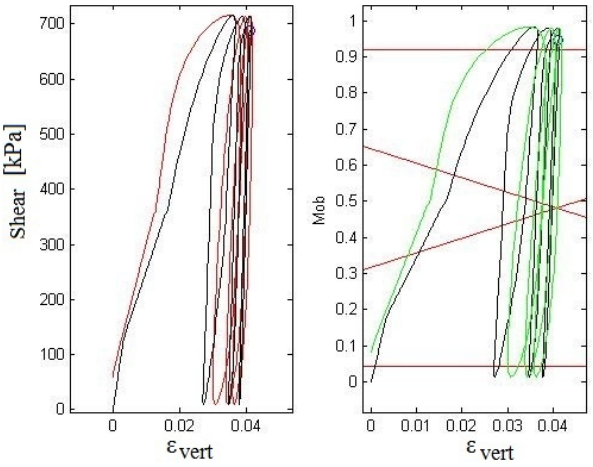

Figure 50. One-way loading simulation of explicit TSP-based model proposed.

In Figure 49 stress-strain curve and Mob-ε plot are shown. The black line is the simulation and the color line illustrates the data recorded during test no. 21 in Table 1.

Figure 50 shows simulation results of a couple of cycles with the same parameters as in Figure 49. Only the loading is changed. One-way loading even though being the most important to capture in terms of increasing shear strength is at the same time the easiest case to fit with reliable parameters for the model.

Symmetric loading case in Figure 51 is slightly corrected to fit to the observed level. A minor adjustment to get the return path acts properly in a single element test case.

Fine tuning the model is rather complicated, methods based on least squares fitting, gradient descent and pattern recognition can be used. The up side is that the shapes captured can potentially be adopted to any case where the minimum and maximum loads are known, covering the full spectrum of 90 % dense Aalborg university sand no. 1 reactions.

9. Conclusion

The ultimate strength in undrained regime is reliably predictable with a linear Mohr-Coulomb envelope. Depending on the loading regime the change in effective friction angle can either increase or decrease the strength of the soil. At all times the ultimate undrained shear strength is located in the point where failure envelope is crossed by the total stress path during cavitation, $TSP + u_{cav}$. This is found to be an extremely consistent and reliable way of estimating undrained shear strength of dense sand.

Undrained one-way cyclic loading on dense sand $I_D = 90$ % can cause strengthning by up to 30 % without increasing its density. It is thought to be due to changes in grain distribution and it is observed to stay after restoring the initial conditions, i.e., after the storm has passed and the excess pore pressure

has dissipated. Strengthning during one-way cyclic loading sometimes results in pore pressure response similar to that found in a porous rock. Moreover the transition between the state of a dense sand specimen into a porous rock type of structure was observed and described.

Stiffness changes in the soil due to cyclic loading are present. In one-way loading the stiffness of the soil is observed to increase, while during two-way loading the stiffness is observed to decrease until failure. This stiffness change is also present when the initial conditions are restored and should be further investigated.

Two-way loading leads to decreased ultimate undrained shear strength. The stiffness change in two-way loading depends on the loading applied. Liquefaction is a common behaviour in two-way loading at 90 % relative density sand.

The possibility to build a material model that can capture the behaviours observed is suggested in this paper in which a very primitive explicit TSP-based material model is presented. This uses the modified mobilization factor, *Mob*, which allows to scale the soil response.

References

Knut H Andersen. Bearing capacity under cyclic loading-offshore, along the coast,and on land. the 21st bjerrum lecture presented in oslo, 23 november 2007. *Canadian Geotechnical Journal*, 46(5):513–535, 2009.

Knut H Andersen and Toralv Berre. Behaviour of a dense sand under monotonic and cyclic loading comportement d'un sable dense sous chargement monotonique et cyclique. In *Geotechnical Engineering for Transportation Infrastructure: Theory and Practice, Planning and Design, Construction and Maintenance: Proceedings of the Twelfth European Conference on Soil Mechanics and Geotechnical Engineering, Amsterdam, Netherlands, 7-10 June 1999*, volume 2, page 667. CRC Press, 1999.

Benjamin Cerfontaine, Robert Charlier, and Frédéric Collin. Possibilities and limitations of the prevost model for the modelling of cohesionless soil cyclic behaviour. In *Proceedings of the 18th International Conference on Soil Mechanics and Geotechnical Engineering*, 2013.

Johan Christian Clausen and Lars Damkilde. A simple and efficient fem-implementation of the modified mohr-coulomb criterion. In *Nordic Seminar on Computational Mechanics*, pages 214–219, 2006.

Sam Helwany. *Applied soil mechanics with ABAQUS applications*. John Wiley & Sons, 2007.

Lars Bo Ibsen. Development of pore pressure and material damping during cyclic loading. In *Dynamics of Structures: a workshop on dynamic loads and response of structures and soil dynamics*, 1991.

Lars Bo Ibsen. The stable state in cyclic loading. In *6th International Conference on Soil Dynamics & Earthquake Engineering*, 1993.

Lars Bo Ibsen. The stable state in cyclic triaxial testing on sand. *Soil Dynamics and Earthquake Engineering*, 13(1): 63–72, 1994.

Lars Bo Ibsen. The static and dynamic strength of sand. Technical report, Geotechnical Engineering Group, 1995.

Lars Bo Ibsen and Ulrik Praastrup. The danish rigid boundary true triaxial apparatus for soil testing. *ASTM geotechnical testing journal*, 25(3):254–265, 2002.

Lars Bo Ibsen, Mats Hanson, T Hjort, and M Thaarup. Mc-parameter calibration of baskarp sand no. 15. Technical report, Aalborg University. Department of Civil Engineering, 2009.

Kenji Ishihara. *Soil behaviour in earthquake geotechnics*. Oxford University Press, 1996.

C LeBlanc, O Hededal, and LB Ibsen. A modified critical state plasticity model for sand-theory and implementation. *Submitted for publication*, 2008.

Søren Kjær Nielsen, Lars Bo Ibsen, Kris Wessel Sørensen, Amir Shajarati, et al. Undrained cyclic behaviour of dense frederikshavn sand. In *The Twenty-third International Offshore and Polar Engineering Conference*. International Society of Offshore and Polar Engineers, 2013.

U Praastrup, Lars Bo Ibsen, and Poul V Lade. A generic stress surface introduced in the customized octahedral plane. Technical report, Geotechnical Engineering Group, 1999.

Amir Shajarati, Kris Wessel Sørensen, Søren Kjær Nielsen, and Lars Bo Ibsen. Manual for cyclic triaxial test. Technical report, Aalborg University. Department of Civil Engineering, 2012.

Alberto Troya and Tomas Sabaliauskas. Post-cyclic undrained behaviour of dense aalborg university sand no. 1. Master's thesis, Aalborg University, Department of Civil Engineering, 2014.

Alberto Troya, Tomas Sabaliauskas, Søren Dam Nielsen, and Lars Bo Ibsen. *Cyclic behaviour of undrained dense Aalborg University sand no. 1*. DCE Technical Memorandum. Department of Civil Engineering, Aalborg University, 2014.

Zhaohui Yang, Ahmed Elgamal, and Ender Parra. Computational model for cyclic mobility and associated shear deformation. *Journal of Geotechnical and Geoenvironmental Engineering*, 129(12):1119–1127, 2003.

Zhao Yangsheng, Hu Yaoqing, Wei Jingping, and Yang Dong. The experimental approach to effective stress law of coal mass by effect of methane. *Transport in porous Media*, 53 (3):235–244, 2003.

ISSN 1901-7278
DCE Technical Memorandum No. 43